Synthesis and Characterization of Fe_3O_4@CNT & its Transport Properties

A Thesis

Submitted towards the partial fulfillment of
BS-MS dual degree programme by

Janani R.G.

November, 2023

under the guidance of

Dr. Ashna Bajpai

Associate Professor, Physics

Indian Institute of Science Education and Research Pune
Dr. Homi Bhabha Road,
Pashan, Pune 411008, India

Certificate

This is to certify that this dissertation entitled "Synthesis and Characterization of Fe_3O_4@CNT & its Transport Properties" towards the partial fulfillment of the BS-MS dual degree program at the Indian Institute of Science Education and Research, Pune represents work carried out by Janani R.G. at IISER Pune under the supervision of Dr Ashna Bajpai (Associate Professor, Physics) during the academic year 2022-23.

09-01-24

Dr. Ashna Bajpai

Committee:
Dr Ashna Bajpai
Dr Surjeet Singh

This thesis is dedicated to my parents, brother, and friends.

Declaration

I hereby declare that the matter embodied in the report entitled "Synthesis and Characterization of Fe_3O_4@CNT & its Transport Properties" are the results of the work carried out by me at the Department of Physics, Indian Institute of Science Education and Research, Pune under the supervision of Dr. Ashna Bajpai, and the same has not been submitted elsewhere for any other degree.

Janani R. G.

Acknowledgements

I would like to express my deepest gratitude to my advisor Dr. Ashna Bajpai, who has been instrumental in guiding, encouraging, and supporting me throughout my research work. I am deeply grateful for her expertise and enthusiasm for the subject matter, which has inspired me and played a significant role in shaping my work.

I would also like to express my appreciation to the Department of Physics at IISER Pune for providing me with the necessary resources, facilities, and funding that made this research possible.

Furthermore, I extend my sincere thanks to my research colleagues, Amit Vishwakarma and Ajad Kumar, Sumedh Gharwade and technical staff members, Nilesh Dumbre, Anil Prathamshetti, Sudhir Lone, and Karthikeyan S., for their valuable insights and feedback that contributed to making the research process a collaborative and enjoyable experience.

Lastly, I am grateful to my family and friends for their unwavering support and encouragement throughout my academic journey. Their love, motivation, and understanding have been a constant source of strength and inspiration, and I could not have accomplished this without them.

I thank everyone for being a part of this incredible journey.

Contents

List of Figures

Abstract

Magnetite is a well-known ferrimagnetic material with a metallic cubic inverse-spinel structure at room temperature and a high Curie temperature of 858K. Magnetite also possesses a low-temperature phase transition known as the Verway transition, at 120K. Below the Verwey transition, magnetite adopts a monoclinic structure and exhibits changes in its electrical magnetic and thermal properties. Fe_3O_4 is a ferrimagnetic oxide of iron, which has numerous practical applications. The present work is about encapsulation of magnetite inside multiwalled carbon nanotubes.

First part of the project synthesis and scaling up of Fe@CNTs was done using the Chemical vapourization method (CVD). The produced CNTs were characterized using X-ray diffraction (XRD), Raman Spectroscopy, Field-Emission Scanning Electron Microscopy (FESEM) and High-Resolution Transmission Electron Microscopy (HR-TEM) for structure, composition and morphology of the Carbon nanotubes and the encapsulate. The CVD-synthesized and characterized sample was used to make a pellet of about 8mm diameter and 2mm thickness and oxidised in a CO_2 environment to produce Fe_3O_4@CNT, which were again characterized using the above-mentioned techniques. Rietveld Refinement, which is a structural refinement process was carried out on the XRD profile of the Fe_3O_4@CNTs to confirm the phases present and composition of the sample.

Fe_3O_4@CNT pellet was used like a pencil to write between two gold contacts on a Printed Circuit Board (PCB). This writing creates a clean electrical path of Fe_3O_4@CNTs between the gold contacts. This can be seen as Fe_3O_4@CNT pellet is made up of CNT ink, which can be used to write between two gold contacts to make an electrical path which allows for electrical conductivity between them. A Closed cycle Refrigerator (CCR) was used for obtaining temperature variation of resistance in the temperature range of 5 - 300 K in the interest of probing the Verway transition and other transport properties of Fe_3O_4@CNT. Studies on Fe_3O_4 thin films of 85nm thickness have shown a change in resistivity of about 3 to 4 orders of magnitude over the range of 50 - 300 K. However, the bare nano-particles of Fe_3O_4 in ultra small (<15 nm) range have shown suppression of Verwey transition. Multiwalled CNTs, on the other hand, typically show resistance decreasing with temperature in the range 5-300 K.

In our case, where Fe_3O_4 nanoparticles are encapsulated inside carbon nanotubes, we find that the resistance still decreases with increase in temperature in the range of 5-300 K. Thus we still find semi-conducting-like behaviour in Fe_3O_4@CNT. We do not find any anomaly corresponding to the Verway transition down to 5K. Further, Variable-Hoping Range (VRH) conduction model fitting was done to the R vs. T data obtained, and we found that 3-D VRH model explains the R vs. T behaviour in a limited range at low temperatures (54 K $<$ T $<$ 100 K). The deviation below 54 K may be due to the interface effects existing between the graphitic shells of CNTs and the Fe_3O_4 encapsulate.

Chapter 1

Introduction

This thesis addresses synthesis, characterisation and electrical transport properties of hybrids based on carbon nanotubes and transition metal oxide magnetite. In the following, the individual constituents of these hybrids are presented.

1.1 Carbon Nanotubes

Carbon Nanotubes (CNTs) are one of the allotropes of the element carbon, which is made up of one dimensional structures. Carbon has allotropes made up of structures with different dimensions- fullerenes which are considered 0-D structures, CNTs are 1-D structures, Graphene is 2-D, and graphite and diamond have 3-D crystalline structure. CNTs consists of sp^2 hybridized orbitals same as in graphite with each atom connected to three other carbons with bond angle 120^o in the x-y plane. Also a weak π-bond is present along the z-axis (In multi-walled CNTs). [46]

Carbon Nanotubes are broadly classified into two types - Single-walled CNT (SWCNT) and Multi-walled CNT (MWCNT). Single-walled CNTs can be imagined as a rolled-up graphene sheet. Typical diameter of single-walled CNTs are 0.4 - 1 nm and the wall is one-atom thick. Multi-walled CNTs are a stack/layers of graphene sheets rolled in the form of a cylinder. MWCNTs can have an outer diameter which can extend up to 100 nm thick. [53] The inter-layer distance in a MWCNT is typically 0.34 nm.

1.1.1 Properties of Carbon Nanotubes

Mechanical Properties

The graphene sheet is made up of carbon atoms in a planar honeycomb lattice. [46] Each atom in it is connected by a strong sp^2 hybridized bond to the neighboring atoms, because of which the elastic modulus of graphite is one of the largest. CNTs are the

strongest known nano-materials in terms of elastic modulus and tensile strength. [54] CNTs have exceptional mechanical properties because of three major forces. CNTs have strong in-plane sp^2 bonds, which gives them their remarkable flexibility both along and off the axis. CNTs can be bent around sharp edges without any breakage. The Young's modulus of single-walled CNT has been reported to be $\sim$ 1.8 TPa. [14, 54] In multi-walled CNT, a weak inter-layer π-bond interaction also exists between the layers, due to which the effective Young's modulus reduces to just a few GPa. [14, 54] CNTs can even withstand non-linear deformations.

Electronic Properties

The electronic properties of CNTs are very similar to that of graphene. Since graphene is a 2-D structure with sp^2-hybridized orbitals of carbon atoms, that gives rise to a zero band-gap semiconductor. [46] The electronic properties of carbon nanotubes are also majorly the effect of sp^2- hybridized orbitals of carbon atoms. Also, the geometric structure of the CNTs like the diameter of tube and chirality also has a significant influence on the electronic properties of the CNTs as the band gap depends on the diameter and the chirality. The high aspect-ratio of CNT (length : diameter) gives rise to electrical conductivity at lower weight ratios compared to traditional materials such as carbon black, carbon fiber, etc. This is a great advantage when it comes to integrating nano-electronic devices. [46] Modulations to the properties of CNTs w.r.t. Graphene arises because only preferred k-states are allowed in CNTs. The CNTs can electrically behave either as a semiconductor or as a metal depending on the chirality and the the direction of the axis and the unit vectors describing the 2D graphene lattice. If the allowed sub-bands pass through the K-points, CNT will be metallic, and if otherwise it will be semiconducting. For semiconducting nanotubes, the band gap is inversely proportional to the diameter. In multi-walled CNTs, the mechanism of conductivity becomes a more complex, and the effect of inter-wall interactions are also significant apart from the diameter and chirality of CNTs. Even then the multi-walled CNTs have known to exhibit exceptional electronic properties also a number of devices based on multi-walled CNT have been extensively studied. [46]

Metallic carbon nanotubes have known to possess electric current densities of 109 A cm^{-2}, which is around 1000 times to that of copper. [46] CNTs exhibit a remarkable electrical conductivity which have been theoretically and experimentally studied extensively. [35] Furthermore, the electronic properties of CNTs can be tuned by addition of functional materials inside or on the surface of the CNT. For instance, it is reported that encapsulating an insulator within the core cavity increases the current carrying capacity of the CNTs and this performs very well as heat sinks in nano-electronic devices. [2] CNTs

are one of the most promising candidates to be used in the designing of nano-electronic devices. Metallic CNTs have been efficiently used as interconnects in integrated circuits. CNTs have been used effectively in various ways, such as, panel displays, scanning probe microscopes, sensing devices, energy science, and other areas of technology. [4, 15, 34, 37, 59, 60]

Thermal Properties

CNT are known to be exceptionally good thermal conductors along the tube axis and good insulators perpendicular to the axis of the tube. [23, 24] CNTs possess almost zero in-plane thermal expansion due to the strong in-plane sp^2 hybridized C-C bonds, which gives them high adaptability against strains along the non axial direction. The thermal conductivity of CNTs also depends on factors such as the number of graphitic shells, its diameter, length and the defects in the lattice. [23, 24] Measurements on individual single-walled CNTs have shown a thermal conductivity of 3500 W $m^{-1}K^{-1}$ at room temperature along its axis. This is around ten times larger as compared to copper, which has a thermal conductivity of 385 W $m^{-1}K^{-1}$. [23, 24] These exceptional thermal properties have applications in nanoscale electronics, sensing devices, etc., and have been investigated extensively. [24, 60]

1.1.2 Conventional Synthesis Methods for Carbon Nanotubes

Laser Ablation Method

In this method, a pulse laser vaporizes the graphite target in a high-temperature reactor in which an inert gas is pumped into to maintain an inert environment. The CNTs formed will deposit on the cooler surfaces of the reactor. CNTs were first synthesized using Laser Ablation method with the help of a dual-pulsed laser. This yielded CNTs of more than 70% in weight purity. [20, 50] Since two consecutive laser pulses are used, the soot carbon after synthesis is significantly reduced. The bigger particles ablated by the initial laser pulse are removed by the second laser pulse. The CNT synthesized will be like a mat of ropes, which are around 100 µm in length, where each rope is a bundle of single-walled CNTs. The CNTs produced are around 10 to 20 nm in diameter. The synthesis parameters on which the quality and properties of CNT are dependent are-laser power, chamber pressure, the distance between the target and the substrates etc. [20, 50]

Arc Discharge Method

Here arc-vaporization of carbon rods is employed to synthesize CNTs. Carbon rods are placed end-to-end in an inert gas filled chamber maintained at low pressure. Due to the

discharge the carbon rod evaporates from the surface of one of the carbon electrodes, which produces rod-shaped deposition on the opposing electrode. This method of production of CNTs gives a high yield. Synthesis parameters on which the quality and properties of CNT are dependent are uniformity of the plasma arc and the temperature maintained at the deposit electrode. [9, 12] This method was one of the most convenient ways to obtain CNTs because of its simple procedure. However, this technique yields a complex mixture of different components. An additional step of purification is required to isolate CNTs from the soot and the residual catalyst particles. In this method, both single-walled and multi-walled CNTs with less structural defects and lengths up to 50 µm can be synthesized. Since this method uses higher temperatures for synthesis of CNTs, more than 1700^{o}C, the resultant CNTs have fewer structural defects when compared to the other synthesis methods. [9, 12]

Chemical Vapor Deposition

This is the most popular and convenient method choice to synthesize different types of CNTs- ranging from single-walled, multi-walled, filled CNTs with various morphologies. CVD has mostly replaced the other methods for synthesizing carbon nanotubes. This method can be used to obtain well-formed CNTs in large quantities. This method also allows a reasonable control over the parameters of CNTs like the diameter, length, and filling fraction. [13, 30, 53, 58] The methods to obtain filled and empty CNTs are similar. Both the processes require a hydrocarbon precursor for the formation of the CNT walls, and a catalyst, usually metallic nano-particles which can facilitate the CNT growth. The catalyst can either be on a suitable substrate, or be used in gaseous form. Organometallic compounds are usually preferred and used as a precursor for the catalytic synthesis of filled CNTs, whereas for pristine CNTs (empty ones) an additional hydrocarbon source in the form of liquid or gas is used. [53, 58]

The organometallic family of metallocenes is the most preferred precursor used for obtaining CNTs with the filing of metal particles in its core cavity. [40, 47, 53] Metallocenes are substances with formula M$(C_5H_5)_2$, where M can be iron, cobalt or nickel, and contains both the hydrocarbon source and metallic catalyst particles to facilitate the growth of the CNTs. Metallocenes consist of metal atoms in the center sandwiched between two cyclopentadiene rings. [11] Metallocene is the most popular choice as a precursor because of its relatively low sublimation temperature (150 - 300 ^oC) and suitable thermal decomposition temperature (600 - 900 ^{o}C) which is the same temperature required for CNT formation. [51] Thus the use of metallocene as a precursor for formation of CNTs is an in-situ process which allows the formation of CNTs and filling of the CNTs to be a simultaneous process. The two widely employed CVD methods are for synthesizing

CNTs are Solid State CVD and Aerosol Assisted CVD.

Aerosol Assisted CVD

Aerosol Assisted CVD employs liquid precursors such as benzene, heptane, acetylene, etc. for the synthesis of CNT. This method is most suitable to obtain pristine CNTs with minimum residual catalyst particles. Here the liquid precursor acts as a carbon source and a solvent for the organometallic compounds. In Aerosol Assisted CVD, the liquid precursor solution consisting of hydrocarbon and metallocene are introduced into the reactor zone. The presence of an excessive amount of carbon source in the gaseous phase allows the formation of hollow empty carbon nanotubes. This method is not suitable for preparing filled CNTs with encapsulation of metal particles. [1, 22, 39, 57]

Solid State CVD

In a typical Solid State CVD, a two-zone horizontal furnace is used for the synthesis of CNTs. In the first temperature zone known as the sublimation zone the precursor is positioned in a quartz boat. This zone is maintained at temperature (T_{sub}) near to the sublimation temperature of the metallocene used. [11, 51]The sublimed plumes are carried into the second temperature zone known as pyrolysis zone set at a relatively higher temperature (T_{pyro}) which is conducive for CNT growth. The sublimed plumes are carried to the pyrolysis region using a transport or carrier gas which can be argon, nitrogen or hydrogen. The CNTs get deposited in the pyrolysis region. The CNTs get deposited onto the inner wall of the quartz reactor or suitable substrates placed in the pyrolysis zone of the reactor on which the CNT growth takes place. Commonly used substrates are thin metal oxide layer coated silicon wafers a layer of metal (iron, cobalt or nickel) coating over it. The additional metal layer acts as a secondary catalyst, which improves the filling efficiency of the CNTs. The Solid-State CVD method is a convenient way to synthesize Carbon Nanotubes (CNTs) that have ferromagnetic metal filling in their core cavity. This process involves growing CNTs in the presence of metal nanoparticles that act as catalysts for CNT growth and provide metal atoms for filling the CNT cores. By varying the synthesis parameters such as temperature, pressure, gas composition, and metal particle size, the filling efficiency and morphology of the CNTs can be tuned. [28] This method results in CNTs with higher filling factors and larger magnetization, which can be useful in a range of applications including magnetic storage, sensors, and biomedical devices. [18, 32, 40, 47, 53]

1.2 Properties of Fe_3O_4 (Magnetite)

Magnetite is a black substance exhibiting ferrimagnetism. Its chemical formula, Fe_3O_4, corresponds to a cubic inverse spinel lattice structure. In this structure, there is a cubic

close-packed arrangement of oxide ions. Half of the octahedral sites are occupied by Fe^{2+} ions, while the remaining octahedral and tetrahedral sites are equally divided among Fe^{3+} ions. Ferrimagnetism in Fe_3O_4 results from the coupling of electron spins in Fe^{2+} and Fe^{3+} ions within the octahedral sites and the coupling of Fe^{3+} ion spins in tetrahedral sites, which are antiparallel to the former. As a consequence, the magnetic contributions from these two sets of ions are unbalanced, leading to a permanent magnetism. Fe_3O_4 exhibits ferrimagnetism with a high Curie temperature of 858 K (585 °C). [6, 19]

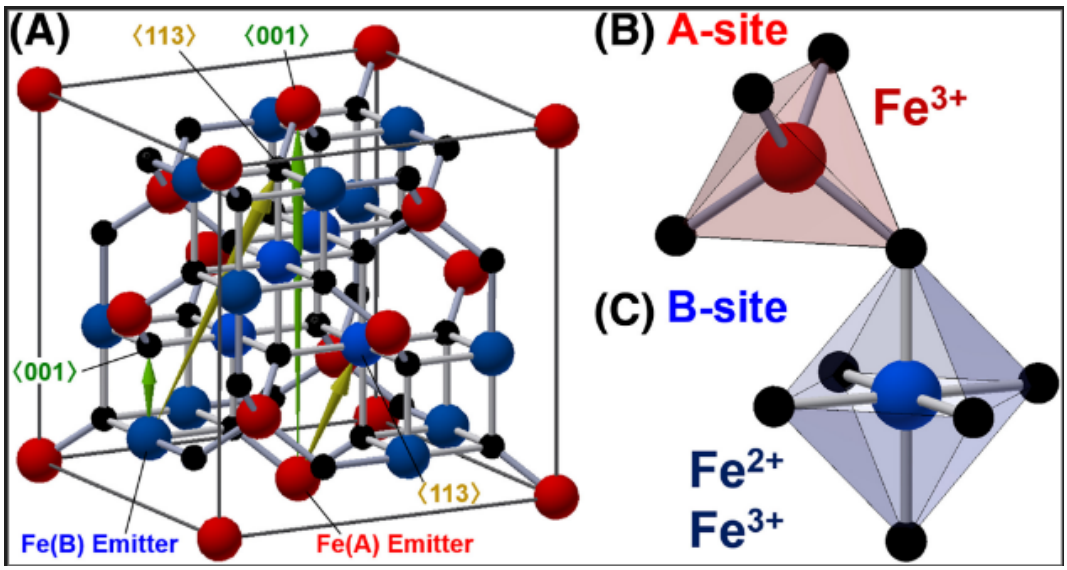

Figure 1.1: Lattice structure of Fe_3O_4 - Cubic inverse spinel structure

At approximately 120 K (-153 °C), Fe_3O_4 undergoes a low-temperature phase transition known as the Verwey transition. During this transition, there is a discontinuity in the structure, conductivity, and magnetic properties. This phenomenon has been extensively studied, and although various explanations have been proposed, it remains not fully understood. Despite having higher electrical resistivity compared to iron metal, Fe_3O_4 possesses a significantly lower electrical resistivity than other iron oxides like Fe_2O_3. This characteristic is attributed to electron exchange interactions between the Fe^{2+} and Fe^{3+} centers within Fe_3O_4. [25, 52]

1.3 Magnetism in Solids

1.3.1 Magnetisation and Magnetic Ordering

Magnetization in Solids

A magnetic material is made up of many atoms, each of which has a magnetic moment. The net magnetic moment per unit volume of the magnetic sample is known as the mag-

netization, or M. Induced magnetization (B) is the result of a magnetic sample being exposed to a magnetic field (H). B and H's relationship is a characteristic of the substance. For materials that are linearly magnetic, such as diamagnets and paramagnets, the relation is given by:

$$B = \mu_0(H + M) \tag{1.1}$$

the magnetic susceptibility of a material is given by:

$$\chi = \lim_{H \to 0} \frac{M}{H} = \frac{\partial M}{\partial H} \tag{1.2}$$

subsubsectionMagnetic Ordering in Solids The ordering of magnetic moments of electron spin structures within a material causes leads to the phenomena of magnetism. Strong interactions are present between atomic magnetic moments, which can be due to exchange interactions or electrostatic interactions.

The migration of electrons around atomic nuclei causes different magnetic interactions to arise within the matter.

1. Orbital magnetic moment resulting from the electron's orbital motion, which is the main factor contributing to the magnetic moment of electrons.

2. A spin moment that is solely attributable to the nature of quantum mechanics and is related to the spin of the electrons.

Long-range magnetic orders are created when magnetic moments in a solid communicate with one another due to magnetic interactions. These interactions can include anisotropic exchange, double exchange, direct exchange, indirect exchange, and magnetic dipolar exchange, among others. Different magnetic ordered ground states can be revealed through competition between these exchange interactions. [5, 17]

1.3.2 Diamagnetism

There is some degree of diamagnetism in all materials. The magnetic moment produced by the external magnetic field in the diamagnetic material tries to repel the external magnetic field. The magnetic susceptibility of the diamagnetic materials is negative and remains constant with temperature variation.

1.3.3 Paramagnetism

Materials with a positive magnetic susceptibility are related to paramagnetism. Magnetic moments within a material have a tendency to line up along an external magnetic

field. Moment alignments are determined at finite temperatures by the conflict between thermal activation energy and the strength of external field. The magnetic susceptibility of a paramagnet diminishes with temperature and is characterized by the Curie-Weiss equation for interacting magnetic moments as:

$$\chi = \frac{C}{T} \tag{1.3}$$

where C is the Curie's constant. This relation is valid at sufficiently high temperatures for weak magnetic fields. [5, 17]

1.3.4 Ferromagnetism

Ferromagnetic substances like Fe, Ni, Co, shows a spontaneous magnetization even in the absence of an applied magnetic field and have a very high magnetic susceptibility. The Curie–Weiss law potrays the magnetic susceptibility χ of a ferromagnet in the paramagnetic region above the Curie point:

$$\chi = \frac{C}{T - T_{\mathrm{C}}} \tag{1.4}$$

where T is the absolute temperature, T_C is the Curie temperature expressed in kelvin bove which a ferromagnetic substance becomes a paramagnet. C is the material-specific Curie constant. The susceptibility will reach singularity at $\mathrm{T} = \mathrm{T}_C$, according to the law. The ferromagnet exhibits spontaneous magnetization below this temperature. [5, 17]
This might be attributed to already-existing close-by interactions between magnetic moments in ferromagnetic order. Heisenberg demonstrated that the electrostatic interactions between interacting electrons might be the source of magnetic order. Pauli's exclusion principle prohibits two electrons from occupying the same quantum state. There are two distinct types of quantum mechanical interactions which take place are:

1. Direct exchange- in which nearby unpaired electrons' wavefunctions significantly overlap with each other.

2. Indirect exchange- when magnetic moments are connected across relatively long distances by a non-magnetic atoms.

[5, 17]
Hamiltonian for exchange interaction for ferromagnets can be described as:

$$H = \sum_{i,j} J_{ij} S_i . S_j \tag{1.5}$$

where i, j are magnetic moments, J_{ij} is the exchange integral which represents coupling strength between the magnetic moments i and j. Ferromagnetic materials has a strictly positive ecxchange integral J_{ij} which is explained by Weiss model. [5, 17]

1.3.5 Anti-Ferromagnetism

Neighboring spins that are anti-parallel to one another are aligned to create an antiferromagnetic magnetic order. Transition metal oxides like MnO, NiO, Fe_2O_3, are some of the most common antiferromagnets (AFM). The exchange energy here is negative which is explained by Weiss theory of antiferromagnetism, which allows the molecular field to be split into two sublattices A and B, each with magnetization M. Magnetic moments in one of the sublattice point upward, whereas they do the opposite in the other. Exchange integrals within a single sublattice are positive, whereas coupling with respect to the other sublattices is negative. In many oxides, where magnetic ions are isolated from one another by oxygen, indirect exchange mechanisms like Double exchange and Super-Exchange interactions can result in Anti-ferromagnetic ordering.[**Coronado1996**]

In AFMs, the temperature above which antiferomagnetic ordering disappears and the material exhibits paramagnetism is known as Neel temperature (T_N). Antiferomagnets obey Curie-Weiss law:

$$\chi = \frac{C}{T - T_{\mathrm{N}}} \tag{1.6}$$

1.3.6 Ferrimagnetism

A ferrimagnetic substance is a material characterized by the presence of atoms with opposing magnetic moments, much like antiferromagnetism. However, in ferrimagnetic materials, these magnetic moments have different strengths, resulting in the preservation of spontaneous magnetization. This effect can happen when the material comprises various types of atoms or ions within a unit cell, such as a combination of $Fe^(2+)$ and $Fe^(3+)$ in the case of magnetite. In ferrimagnetic substances, magnetization occurs due to interactions between dipoles and exchange interactions that obey the Pauli exclusion principle. [42, 49]

Like ferromagnetic materials, ferrimagnetic materials exhibit attraction to magnets and can be magnetized to create permanent magnets. Magnetite (Fe_3O_4), the earliest known magnetic substance, was initially classified as a ferromagnet until Louis Néel discovered ferrimagnetism in 1948. Since its discovery, ferrimagnetic materials have found numerous applications, including in hard drive platters and biomedical uses.

Ferrimagnets also exhibit a critical temperature, known as the Curie temperature, above which they transition to a paramagnetic state, similar to ferromagnets. At this temperature, a second-order phase transition occurs, and the material can no longer maintain spontaneous magnetization. This loss of magnetization is due to the increasing strength of thermal motion at higher temperatures, overcoming the tendency of dipoles to align. [42, 49]

1.3.7 Half-Metallic Materials

Half-metal is a material that conducts electrons with one spin direction effectively, while it behaves as an insulator or semiconductor for electrons with the opposite spin direction. In half-metals, the valence band is partially occupied for one spin direction, while there exists a gap in the density of states for the other spin direction. Consequently, only electrons with the first spin direction exhibit conducting properties. One of the most famous example of half-metals is Fe_3O_4. [16, 26]

Chapter 2

Experimental Methods

2.1 Characterization Techniques

2.1.1 Powder X-Ray Diffraction

Powder X-Ray Diffraction (PXRD) is a well known technique primarily used for qualitative and quantitative analysis of the crystalline phases of materials. XRD patterns can reveal information such as unit cell dimensions, crystallite size and shape, crystal orientation, close surface characterization, characterization of solid solutions etc. The constructive interference of monochromatic X-rays on the lattice planes of the crystalline sample allows us to characterize diffrent crystalline substances.

Bragg's Law: Bragg's Law establishes that when a monochromatic X-ray beam is directed at a crystal surface at an angle of incidence (θ), it will be scattered at the same angle (θ) due to the regular arrangement of atoms in the crystal lattice. If the path difference (d) between the X-ray waves is proportional to an integer multiple (n) of the wavelength (λ), the waves will constructively interfere, resulting in a diffraction pattern. The mathematical expression that defines Bragg's Law precisely is:

$$2d \sin\theta = n\lambda \tag{2.1}$$

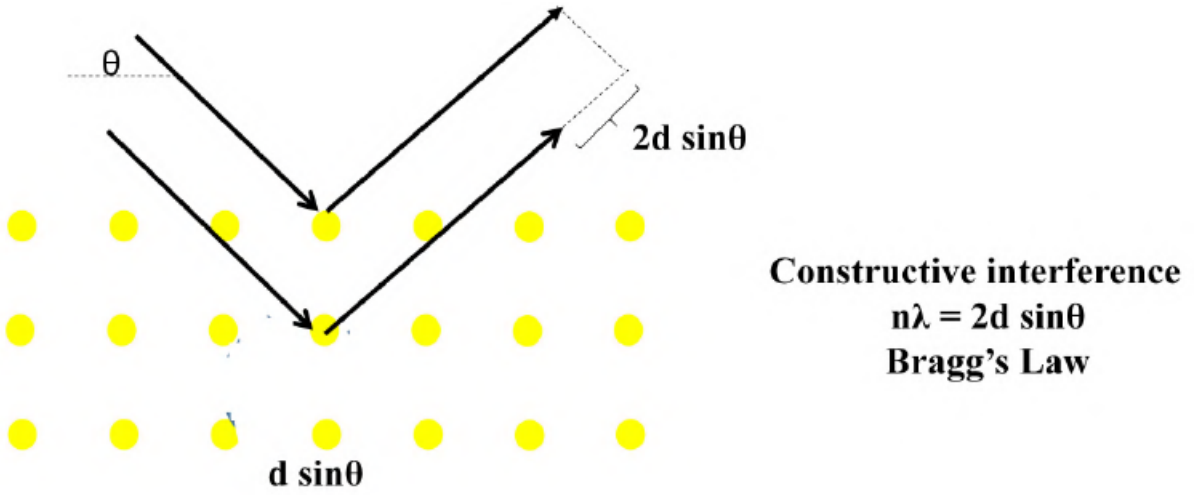

Figure 2.1: Schematic Representaion of Bragg's Law [21]

The cathode ray tube generates a broad spectrum of X-rays, which are then filtered to produce monochromatic radiation of a specific wavelength. The collimator is used to focus and direct the X-rays towards the sample, which is mounted on the goniometer. The diffracted X-rays are collected by the X-ray detector, which is mounted on another arm that rotates at an angle of 2θ relative to the sample. By scanning the detector at different angles, the X-ray diffractometer can collect a complete diffraction pattern that can be analyzed to determine the crystal structure of the sample. [21]

2.1.2 Rietveld Refinement

Rietveld refinement, pioneered by Hugo Rietveld, is a technique employed in the analysis of crystalline substances. When neutron and X-ray diffraction is applied to powdered samples, it generates a distinct pattern characterized by reflections, which are peaks in intensity occurring at specific positions. By examining the height, width, and position of these reflections, various details about the material's structure can be deduced.
The Rietveld method utilizes a least squares approach to fine-tune a theoretical line profile until it closely matches the actual measured profile. This technique optimizes user-selected parameters to minimize the disparity between observed data and a model constructed based on the assumed crystal structure and instrumental factors. It simultaneously refines the observed diffraction pattern using theoretical models that consider elements such as crystal structure, diffraction optics, instrumental characteristics, lattice parameters, and more. [45]

Principle of Rietveld Refinement

The powder diffraction pattern is recorded as numerical intensity value y_i in the incremental steps i. The increments here is scattering angle 2θ. The 'best fit' is the best least squares fitting to accommodate all the y_i simultaneously. Residual function S_y is the quantity to be minimised, which is given by: [45]

$$S_y = \sum_i w_i (y_i - y_{ci})^2 \tag{2.2}$$

where, $w_i = 1/y_i$, y_i is the observed intensity at every i^{th} step, y_{ci} is the calculated intensity at the $i(th)$ step.

The background intensity y_{bi} at the i^{th} step can be obtained from either an user supplied file, or linear interpolation of the user selected points, or a specific background function. Background function is generally a sixth-order polynomial function and can also be an input from the user in the form of user generated .bg file with refinable heights. The reflection profile function ϕ approximates the effects of instrumental features as well as sample's features. The reflection profiles available in most of the programs include two different pseudo-Voigt functions, Gaussian, Pearson VII, Lorentzian and modified Lorentzian functions. We have used pseudo-Voigt function in refining the data presented in this thesis.

The dependence of the the breadth H in the reflection profile is described by Caglioti's formula written as: [45]

$$H^2 = U\tan(\theta)^2 + V\tan(\theta) + W \tag{2.3}$$

where U, V, W are hte refinable parameters which defines the peak width and the peak shape of the reflection profile.

The Lorentz-Polarization factor L_K takes care of the instrumental factors. The scattering of the light from the atom and diffracted light from the monochromator to remove unwanted wavelengths of radiation can polarize the X-ray beam. These factors are included in the Lorentz-Polarization factor L_K. [45]

Procedure for refinement

The Rietveld refinement for the samples investigated in this thesis were done on "FullProf" software. The input files are the experimental data in .dat file, and crystallographic

information in .cif file which contains the crystallographic information about the crystal. CIF file for each phase of compound has to be uploaded. After the input of the files, and manually adding/adjusting parameters such as wavelength of the X-ray source, background function/external background file, type of reflection profile function, the program is run for refinement.
The sequence followed for refinement for a crystal structure is as follows.

1. Scale factor.
2. Scale factor, zero point of detector, background parameter and instrumental parameters. The background was fixed using linear interpolation with a set of pre-decided points provided by user.
3. Refine the lattice parameters - a,b,c.
4. Atomic positions.
5. Refine the peak shape (U, V, W) and asymmetry parameters (if necessary).
6. Add atomic occupancies.
7. Add preferred orientation(if necessary).
8. Refine for the overall Debye-Waller factor.
9. Micro-structural parameters: size and strain effects.

2.1.3 Field-Emission Scanning Electron Microscopy

The Field-Emission Scanning Electron Microscopy (FESEM) involves the liberation of electrons from a field emission source, which are then accelerated in a high electrical field gradient within a high vacuum column. These electrons are referred to as primary electrons. The primary electrons are subsequently focused and deflected by electronic lenses to generate a collimated and focused beam that is used to bombard the object. This results in the emission of secondary electrons from the sample. The surface morphology of the object is related to the angle and velocity of these secondary electrons. An electronic signal produced by the secondary electrons on the detector, and it is then amplified and converted to a scan-image or video for display on a monitor. The resulting image is an intensity distribution map of the electrons emitted from the sample. For effective visualization under SEM technique, it is preferable for the sample to be conductive to allow the beam to strike its surface for imaging purposes. [43]

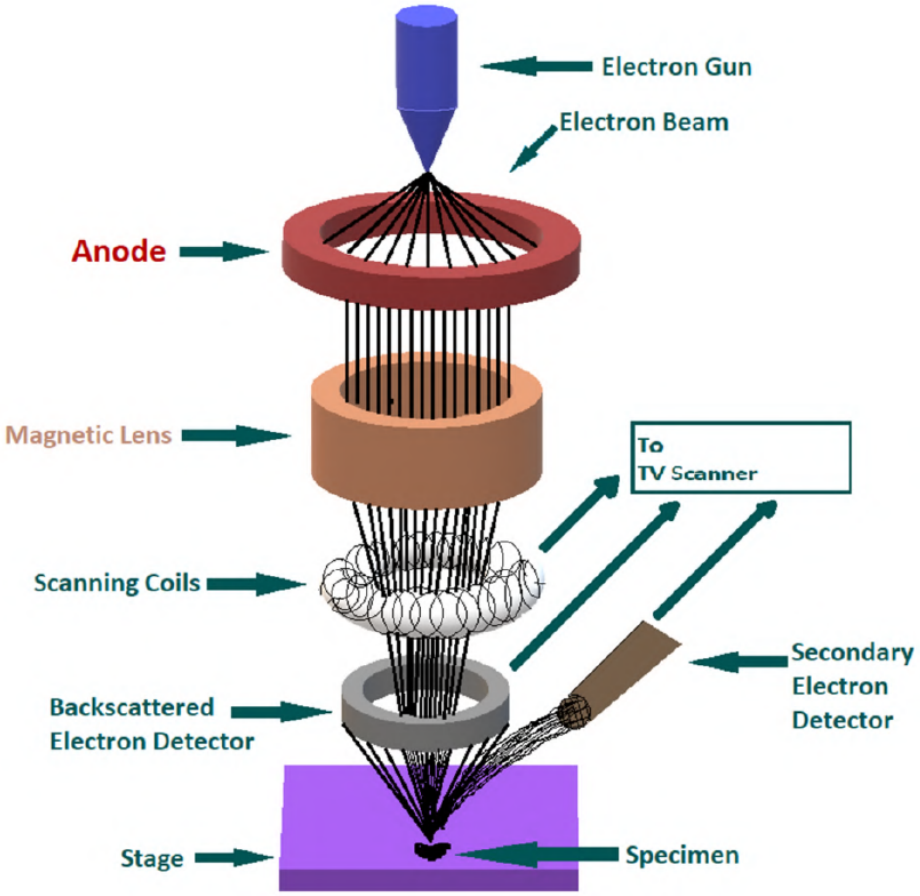

Figure 2.2: Schematic Representation of a SEM instrument [43]

When the secondary electrons are emitted from the inner shells of the atoms, the electrons from the outer shells will fill up the empty inner shells. This transition of electrons will emit x-ray photons with an energy equal to the difference between those energy levels. The wavelengths of these emitted x-ray photons are characteristic to a particular atom, and, therefore, the analysis of these energies of the characteristic X-rays are used to determine the elemental composition of the sample. This technique is known as Energy Dispersive X-Ray (EDX). EDX can provide qualitative and quantitative information of the selected area on the surface of the sample. [43]

2.1.4 Transmission Electron Microscope

Transmission electron microscopes (TEM) uses a beam of electrons to visualize specimens and generate a highly-magnified image. TEM operates almost on the same optical principles as the light microscope. The wavelike behavior of electrons allows a beam of electrons to be focused and Diffracted, and thus imagimg is possible.

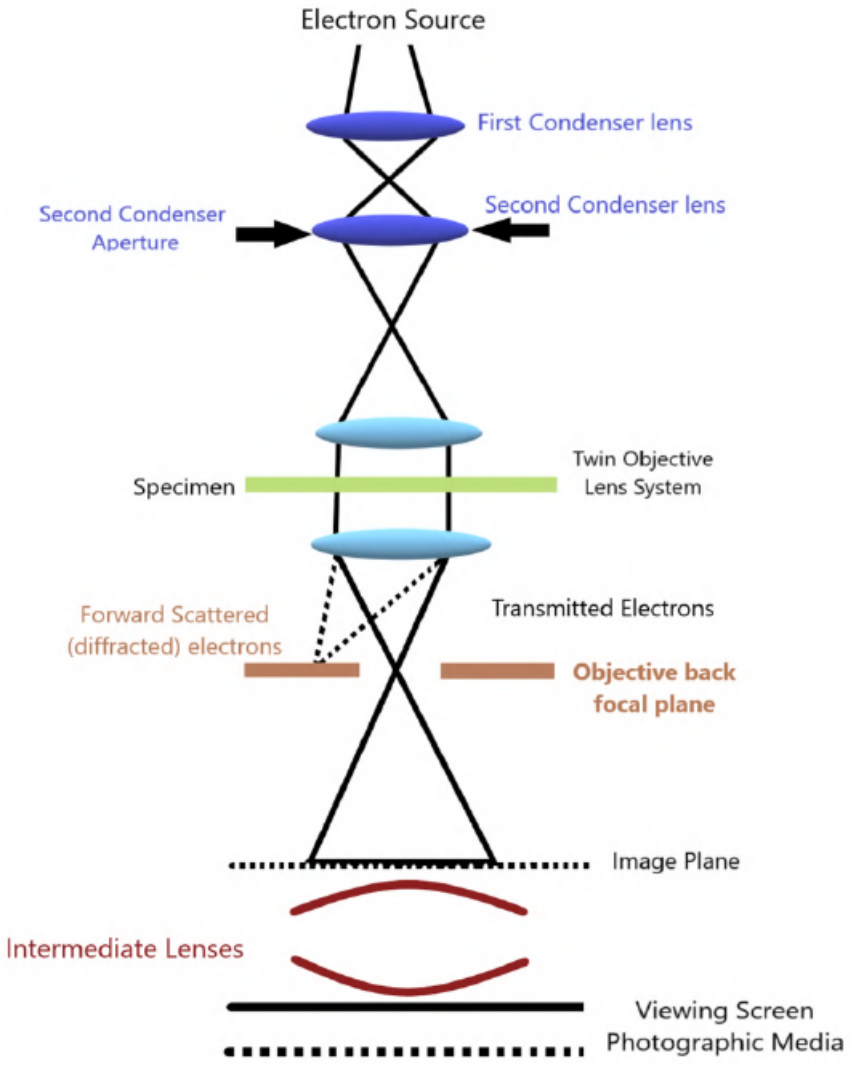

Figure 2.3: Schematic representation of a TEM instrument [7]

The source electrons are generated by thermionic emission from a filament or through field-emission. An electric potential is used to accelerate the electrons, and the accelerated electrons are focused by electrostatic and electromagnetic lenses onto the specimen. The transmitted beam which consists of information about the specimen's electron density is used to form an image. Electrostatic plates are used so that the electrons will be deflected by a constant angle. Different magnetic fields form a magnetic lens of variable focusing power and the lens shape originates due to the magnetic flux distribution. The condenser lenses are basically solenoid or an electromagnet which produces a focused beam of electrons on the sample.. The focusing power of the magnetic lens can be altered by changing the current passing through the solenoid. Also there are lenses which are placed after the sample which is the intermediate lens system. This lens system can be adjusted to form a diffraction pattern or image of the sample with magnification up to 1,000,000x. [7]

2.1.5 Raman Spectroscopy

The way light interacts with materials can result in transmission, reflection, or scattering. To analyze the vibrational modes in a system and gain information on both its chemical and structural characteristics, the technique of Raman scattering is used, which involves inelastic scattering of monochromatic light. This method can also be used to identify (characterize) substances. A typical Raman spectrometer includes a laser source that excites the sample, a filter that delivers monochromatic laser light to the sample, a detector that collects the light and sends it to a spectrograph for measurement of light intensity at various wavelengths, and a microscope that focuses the laser light onto a point on the sample surface. The whole system is controlled by a computer, which handles instrumental control and data manipulation. [8, 10, 31]

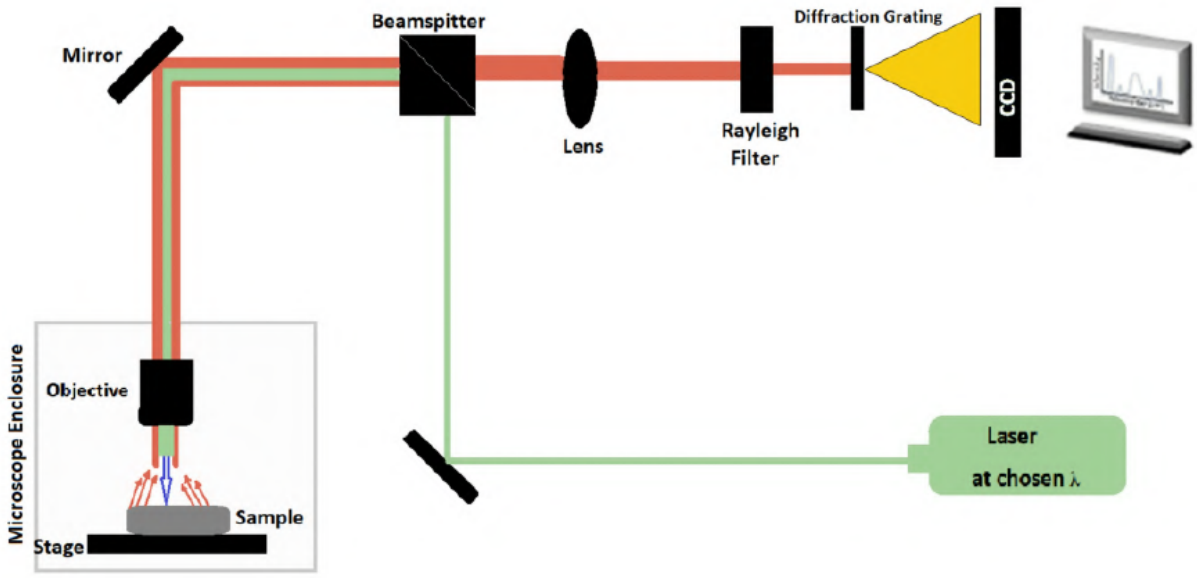

Figure 2.4: Schematic representation of a Raman spectrometer [8]

When a laser beam of monochromatic light interacts with a material, some of the photons are absorbed by the sample and then emitted back. Most of the photons are elastically scattered, which means their energy remains the same as that of the incident photons, and this is referred to as Rayleigh scattering. However, a small portion of the light scatters with a frequency shift either up or down from the incident photons. This inelastic scattering is called the Raman effect. The frequency shifts provide details about the low-frequency transitions, rotational and vibrational patterns in the molecules. [8, 10]

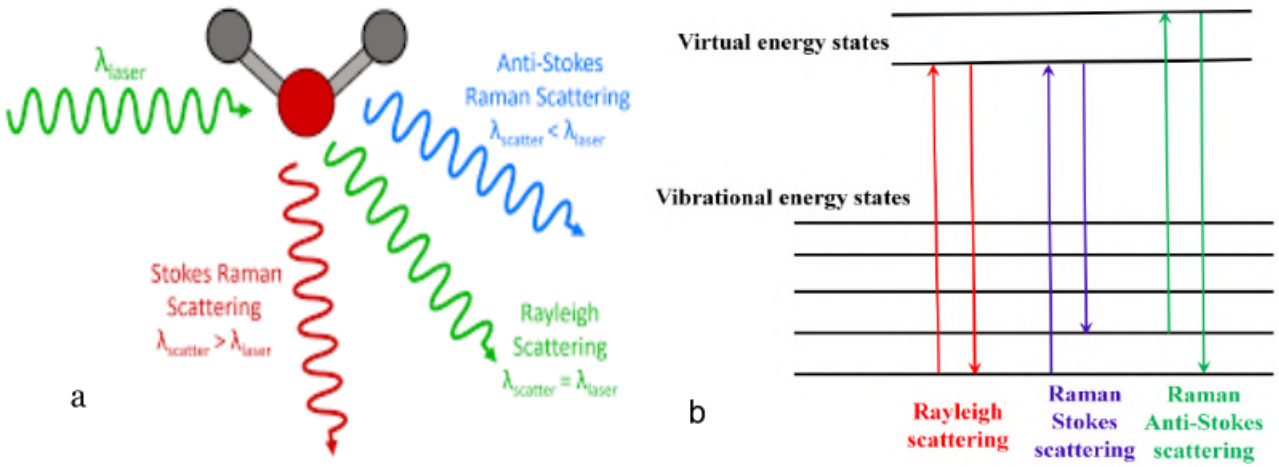

Figure 2.5: a)Schematic image depicting the rules for different scattering b)Energy level diagrams for Rayleigh & Raman Scattering (Stoke and Anti-stokes) [8]

Raman scattering:
When light interacts with a molecule, the oscillating electromagnetic field of a photon creates a polarization of the molecule's electron cloud, causing the molecule to enter a higher energy state. This results in the transfer of energy from the photon to the molecule, and a short-lived complex is formed between them. This complex is known as the virtual state of the molecule, but it is not stable, and the photon is quickly emitted as scattered light. The lines that have a frequency lower than the incident frequency, meaning that the inelastic scattering photons lose energy while creating a photon, are referred to as Stokes lines. On the other hand, the lines with a frequency higher than the incident frequency are called Anti-Stokes lines. The likelihood of these processes occurring is influenced by the excitation energy and temperature. [8, 10]

2.2 Synthesis of Metal Filled Carbon nanotubes

2.2.1 Precursor and parameters for CVD

Chemical vapor deposition (CVD) is one of the most popular method to synthesize single-wall and multi-wall CNTs. In this technique a hydrocarbon precursor compound is used which acts as the carbon source for the CNT synthesis and a catalyst is used which facilitates the growth of the graphitic shells. Organometallic compounds are the most popular choice for catalytic synthesis of filled CNTs, specifically, metallocenes ($M(C_5H_5)_2$), where M can be iron, nickel or cobalt, which are the most commonly used precursors for synthesizing metal-filled CNTs. The metallocene ($M(C_5H_5)_2$) consists of two five membered

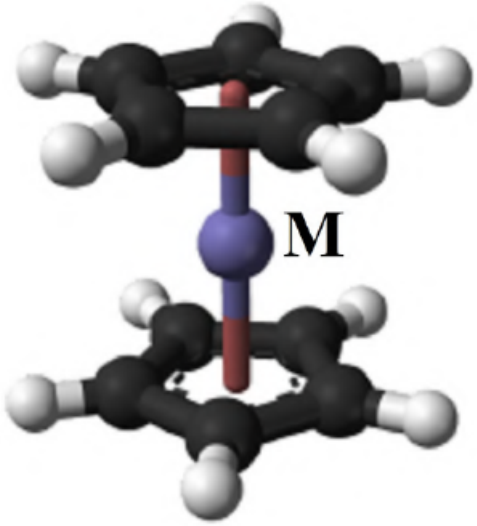

Figure 2.6: Representative image of a molecule of ferrocene. M represents the central metal atom. [27]

cyclic organic molecules bound to a central metal atom. Fig.2.6 is a representation of the general structure of a metallocene molecule. [18, 28, 32, 40, 46, 47]

Using metallocene has an added advantage because these compounds provide both the carbon source and the metallic catalyst particles to facilitate the growth of the CNTs. Metallocenes have a low sublimation temperature (150 - 300 ^{o}C) which makes them one of the most common and convenient choice as a precursor.

In a typical Solid State CVD, a dual-zone furnace is used. Here, the first temperature zone is known as the sublimation zone where the metallocene is sublimated at a specific temperature (sublimation temperature of the precursor) and this is referred to as the "T_{sub}." The metallocene plumes are carried by an inert gas to the second zone which is known as the pyrolysis zone. This zone is maintained at a relatively higher temperature than the sublimation temperature and is referred to as the pyrolysis temperature "T_{pyro}." The precursor gets decomposed and the CNTs grow in the pyrolysis zone according to the other synthesis parameters. The morphology of the CNTs formed critically depends on T_{pyro} and T_{sub}. Therefore, typically a dual-zone furnace with two independent temperature controllers is used so that both the sublimation and the pyrolysis temperature can be controlled accurately. [18, 28, 32, 40, 46, 47]

2.2.2 Single-zone Furnace for Solid-state CVD of metallocene

In our synthesis method, we used a single-zone furnace that has be modified efficiently to fore-go the dual-zone furnace for synthesis of metal and metal-oxides filled CNTs.

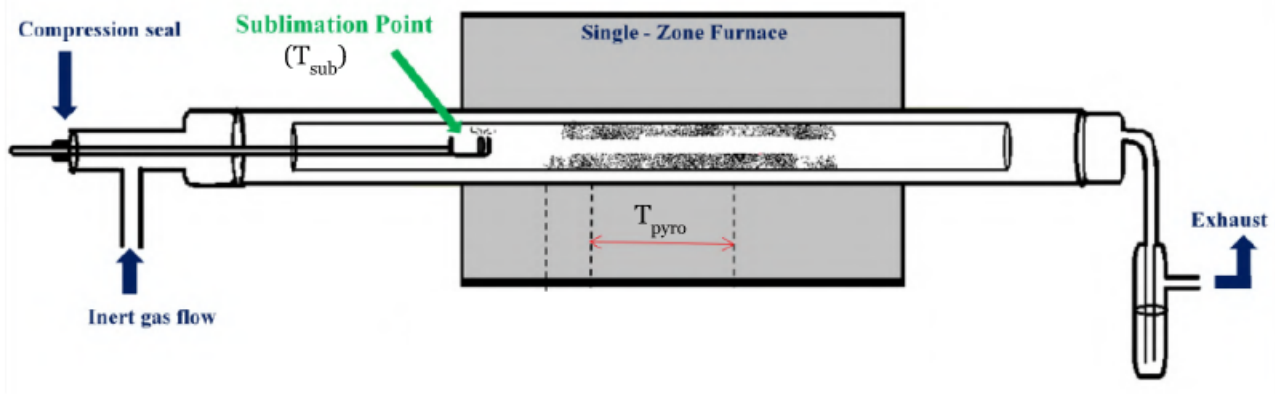

Figure 2.7: Schematic representation of the single-zone furnace with the modified synthesis chamber; taken from [27, 28]

A single-zone horizontal tube furnace from Nabertherm is used which can heat upto a maximum temperature of 1300 ^{o}C. The inner diameter of the ceramic tube furnace is 50 mm and the length of the ceramic tube is 1 m. The temperature profiling was done for the setup at 900^{o}C. The single-zone furnace consists of a constant temperature zone in the middle, which is roughly 60 cm in length with temperature stability of 2^{o}C. Along the two outer sides, the variable temperature zones are present. The middle region with constant temperatureT_{pyro} is used as the pyrolysis region, and the variable temperature zones on either side of the constant zone is used as the sublimation zone.Temperature profiling of the variable temperature zone is made to determine the spot at which the furnace remains in the desired T_{sub}. As shown in 2.7 T_{pyro} region is the constant temperature zone and on either sides of it the variable temperature zone exists. [28]

2.2.3 Carbon Nanotube Synthesis Procedure

The CVD Synthesis Set-up

The CVD setup consists of a synthesis chamber, a compression seal arrangement with the precursor in a quartz boat, and gas flow tube and exhaust tubes. The synthesis chamber consists of two coaxial quartz tubes, where the outer tube is 170 cm in length with inner diameter 37 mm and wall thickness of 3 mm and the inner tube is 1 m in length with 25 mm inner diameter and a wall thickness 3 mm. The inner tube is where the CNTs mainly gets deposited. The outer quartz tube is connected to a standard compression seal arrangement at one side. This allows for the insertion of the precursor i.e. metallocene in powder or solid (pressed pellet) form. A small semi-cylindrical container to place the sample, which is referred to as the sample boat is fused to a long glass rod to facilitate it to be pushed to the predetermined spot in the inner tube in the variable temperature

region. The compression seal arrangement allows the quartz rod to move into the inner quartz reactor of he synthesis chamber with precision without disturbing the inert gas flow. The other end of the quartz tube is connected to the acetone trap to trap any substance which flows out of the synthesis chamber, which is connected to an exhaust. Thus the compression seal arrangement along with the temperature profile of the synthesis chamber allows one to extend the use of a modified single-zone furnace as a dual-zone furnace with suitable T_{pyro} and T_{sub}. This removes the limitation of requirement of a dual-zone furnace for synthesis of filled CNTs, which costs a lot more than the single-zone furnaces. The design of the synthesis chamber and modifications leads to a better control in length, diameter, filling efficiency and morphology of the CNTs produced. [28]

Synthesizing CNTs

The precursor used here is Ferrocene which is 98% pure, procured from Sigma Aldrich. The outer quartz tube is annealed at 800^oC for twelve hours before to every synthesis run. For each run, a new and thoroughly cleaned and dried inner quartz tubes was used. The ferrocene powder was made into a pressed pellet using 500-700 mg of ferrocene powder. The metallocene pellet is be then placed inside the sample boat. The sample boat is positioned such that it remains at room temperature, so that no sublimation of the precursor takes place when the furnace is heated up to 900^oC (Sublimation temperature of ferrocene 150^oC). Before switching the furnace on, the synthesis chamber is flushed with argon gas for a few minutes. A programme is set to heat up the furnace at 800 ^oC per hour from room temperature to 900^oC. Here, 900^oC is a pre-optimised T_{pyro} for the synthesis of iron filled CNTs with aligned forest morphology. When the furnace attains the required fixed temperature ($T_{pyro} = 900^oC$) it is left to stabilised at 900^oC for 15 to 20 minutes. Then the quartz boat is pushed through the compression seal assembly to a pre-determined spot in the synthesis chamber which will have the temperature of T_{sub}. T_{sub} for synthesizing Fe@CNTs with aligned forest morphology was optimised at 300^oC by A. Kapoor. [28] Once the metallocene gets sublimed, the carrier gas, which is the argon gas here, carries the plumes of metallocene to the middle of the synthesis chamber, which is the fixed temperature zone with temperature maintained at T_{pyro}. Reaction time here is 10 to 15 minutes, and the setup held stable for this time after the sample boat is pushed till T_{sub}. Then the furnace is switched off, and is allowed to cool down to room temperature under argon gas flow. Argon gas flow should be at least maintained till $\sim 150^oC$.

Once everything is cooled down, the CNTs formed on the surface of the inner quartz tube is scraped off using a glass rod and then magnetically removed out the tube. The inner tube is divided into sections, and then the sample is retrieved so that the CNTs

formed in the variable temperature zone (temperature varying from 600 - 900 ^oC) and in the fixed temperature zones are not mixed up. The middle section (corresponding to the fixed temperature region) has the best quality of well formed aligned forests of CNTs with minimum residual catalyst particles. The CNTs obtained from the variable temperature region are more distorted, and has higher concentration of residual catalyst particles along with the aligned forests. This also makes it clear that T_{pyro} is very crucial as to the morphology of the CNTs formed.

Important thing to note is that, if the argon gas flow rate is too high, the gas would carry away the submlimed plumes of ferrocene particles away from the fixed temperature region. Also, if the flow rate is too low, the gas would not be able to carry most of the ferrocene particles to the fixed region. This would affect the yield as well the quality of the CNTs formed. Optimal flowrate should be just enought to carry the sublimated ferrocene particles upto the fixed temperature region.

2.2.4 Oxidation Procedure to synthesize Fe_3O_4@CNT

Oxide filled CNTs like Fe_3O_4 filled CNTs are used for applications in batteries and spintronics/ nano-electronics. Spaghetti-like morphology of CNTs is preferred in the case of battery related applications, whereas the alligned forest morphology can be more suitable for nano-electronics/spintronic applications. [28, 55]

Fe@CNTs are converted to α-Fe_2O_3@CNTs and Fe_3O_4@CNTs by annealing them at suitable conditions in carbon dioxide environment . The synthesis chamber for annealing remains the same as for synthesis of Fe@CNT, but no inner quartz tube will be used and the gas flowing in the chamber will be carbon dioxide. Measured amount of Fe@CNT ($\sim$100-150 mg) was made into a pressed pellet. The pellet on a sample boat is placed in the CVD setup such that it remains in the room temperature. Synthesis chamber is then flushed with CO_2 gas for a few minutes, and then the furnace is set to heat upto 500^oCC. Once the furnace reaches 500^oC and stabilises, the sample boat is pushed in so that it will be positioned well inside the fixed temperature region. CO_2 gas flow rate is kept very low, as here it doesn't act as a carrier gas, but only needs to provide a CO_2 environment for the oxidation of iron to take place. Also low gas flow rate ensure that Fe@CNTs won't fly away (carried away by the gas) and reduce the yield of α-Fe_2O_3@CNTs or Fe_3O_4@CNTs.

2.3 Resistivity Measurements

Setup for resistivity Measurement: A Closed Cycle Refrigerator (CCR) which works on the basis of Gifford-McMahon Cycle is connected to Lakeshore 360 Temperature Con-

troller. The Temperature controller stabilizes to a set temperature using a PID controller. The CCR is enabled with ten wires, of which of 2 of them were used for the resistivity measurements. The wires are connected to Keithley 2450 Sourcemeter. The Sourcemeter has sensitivity of 1µV and resolution of 1nA. The Cernox Temperature sensor (Temperature range: 4K to 325K) is mounted near the sample on the sample holder, which gives us the idea of the temperature of the sample.

Sample Preparation and Mounting: A PCB made of epoxy fibreglass with pre-made gold contacts were used. The pellet of Fe_3O_4@CNTs was held and a line was drawn between gold contacts. This created a continuous layer structure of Fe_3O_4@CNTs over the insulating fibreglass and thus making a connection between the gold contacts. This connection made using Fe_3O_4@CNTs creates a percolation path between the two contacts and this makes the path electrically conductive. One or Two clean strokes of Fe_3O_4@CNTs between the contacts had a resistance of about 2.3 kΩ at room temperature.

Chapter 3

Synthesis and Characterization of aligned forests of Fe_3O_4@CNTs

The Solid-state CVD method using ferrocene as a precursor was employed to synthesize the CNTs. The Iron filled aligned forest CNTs were synthesized at T_{sub} of 300^{o}C and T_{pyro} of 900^{o}C which was optimised by A. Kapoor et al. [27, 28] Even though the basic CVD setup was same as A. Kapoor et al, The ceramic tube in the setup was replaced. Thus we had to do a temperature profile for the present setup. Totally eight CVD runs were carried out to scale up the Fe@CNT sample. A pressed pellet of Fe@CNTs was made to carry out oxidation.

3.1 Temperature profiling of the Furnace at 900^{o}C

In order to record the temperature from temperature profiling of the inner chamber, a 1m long K-type thermocouple was used along with a temperature reader. Starting from one end of the furnace, temperature was recorded at 0.5cm intervals till the middle region. With the help of this temperature profile, we were able to determine the exact point at which the temperature of the furnace would be the required sublimation temperature (T_{sub}). So with the help of the temperature profile of the furnace, we could insert the sample boat with the ferrocene precursor to the desired spot of $T_{sub} = 300^oC$.

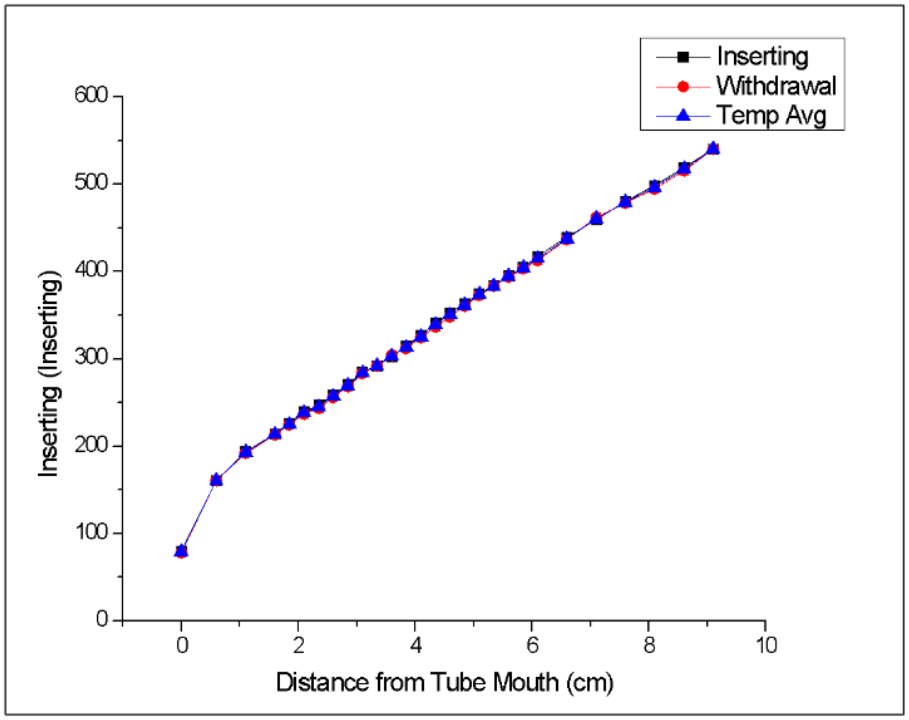

Figure 3.1: Temperature profile of the variable region at 900^{o}C

Due to the limitations of the proper temperature measuring apparatus, we could not record the complete temperature profile of the variable temperature zone till the constant temperature zone (room temperature to 900^{o}C). The Thermocouple we used had a maximum temperature limit of 750^{o}C. Thus, the temperature profile was determined only for the temperature range of 50 - 550 ^{o}C.

3.2 Synthesis and Characterization of Fe@CNTs

Alinged forest Fe@CNTs were synthesised using the Solid-state CVD method optimised by A. Kapoor et al. [28] The most important synthesis parameters in Solid-state CVD are the Sublimation and Pyrolysis temperatures which were T_{sub} = 300^{o}Cand T_{pyro} = 900^{o}C.

T_{sub}, T_{pyro}	Amount of precursor	well-aligned good quality CNTs	Aligned CNTs with higher residual particle density
300^{o}C, 900^{o}C	500 mg	40-70 mg	80-100 mg
300^{o}C, 900^{o}C	700 mg	100-150 mg	150-200 mg

Table 3.1: Amount of precursor to amount of good quality CNTs produced

As we can see from the table 3.1 above, we can see that increasing the amount of precursor for a run from 500 mg to 700 mg gives almost double the amount Good quality

CNTs. The reason for this could be as follows. In order for the sublimed plumes of ferrocene to reach the constant temperature zone, we need to have a good flow of Argon gas. While this ensures most of the sublimed particles reach the constant temperature zone immediately after it gets sublimed, there will be some amount of particles which will get carried far away from the constant temperature region to the other side of the synthesis chamber before it gets a chance to under pyrolysis at 900^oC. Since the Argon gas flow rate and duration of pyrolysis were same for both 500 mg and 700 mg runs, the wastage in the precursor which gets carried away before the reaction will be similar. Argon gas flow rate and the duration of pyrolysis has been optimised to synthesize aligned Forest CNTs and changing these parameters will affect the morphology and quality of the CNTs produced. Instead this way of increasing the precursor will give a better yeild without any compromise in the morphology or the quality of the CNTs produced.

3.2.1 Raman Spectroscopy on Fe@CNT

Pristine multi-walled carbon nanotubes exhibit three distinctive Raman peaks, specifically at wavelengths approximately equal to 1350 cm$^-$1, 1583 cm$^-$1, and 2692 cm$^-$1. These peaks are associated with the D band (representing disorder), the G band (associated with the graphitic shells), and the G' band (corresponding to the second-order harmonic of the G band), respectively. [61]

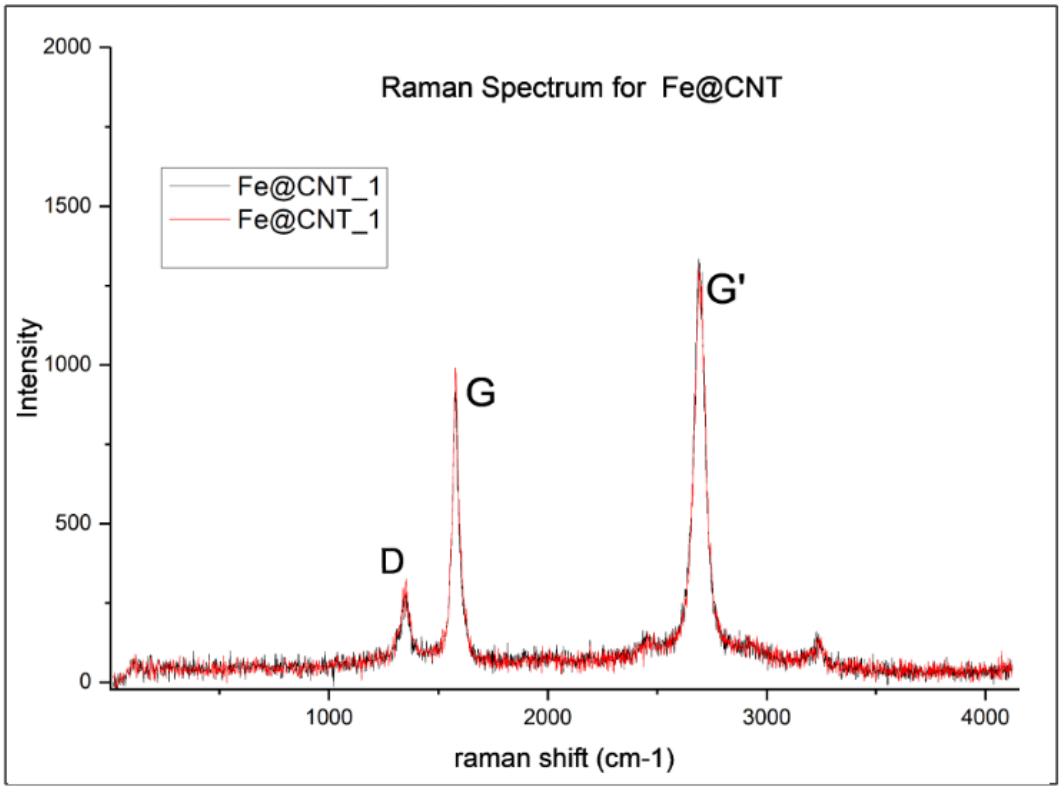

Figure 3.2: Raman Spectrum for Fe@CNT.

Green laser with wavelength of 532 nm was used for the Raman charecterisation. The laser power used was 2mW. The encapsulated Fe particles do not show any significant Raman shift.

3.2.2 FESEM on Fe@CNT

FESEM micrographs of the CNTs at ∼20000x magnification shows the well-formed, alligned carbon nanotubes. It is observed that several carpets of alligned forests of carbon nanotubes are formed. These representative micro-graphs corresponds to the aligned CNTs procured from the constant temperature region. FESEM imaging can only visualise the structure of graphitic shells properly. Iron filling inside the nanotubes are not clearly visible.

Since Fe@CNTs are conductive material, there is no need of any additional coating over the sample in order to visualize them under the FESEM. FESEM images give us the structure and quality of the CNTs formed. In the same instrument, the characteristic X-rays produced are also used to determine the elemental composition of the sample. This technique is known as the Energy Dispersive X-Ray (EDX).

Sample Preparation for FESEM To prepare non-conducting samples for analysis, it is necessary to apply a thin layer of conductive material such like Gold using techniques such as sputter coating or high vacuum evaporation. Additionally, the samples must be able to withstand the high vacuum environment without undergoing changes such as the loss of water molecules or gases. For powder samples like CNTs, a carbon tape is affixed to a stub, and the powder is then sprinkled onto the tape. The stubs are placed in a desiccator with a vacuum pump to remove any particles that have not adhered to the tape, preventing the accumulation of fine particles within the instrument.

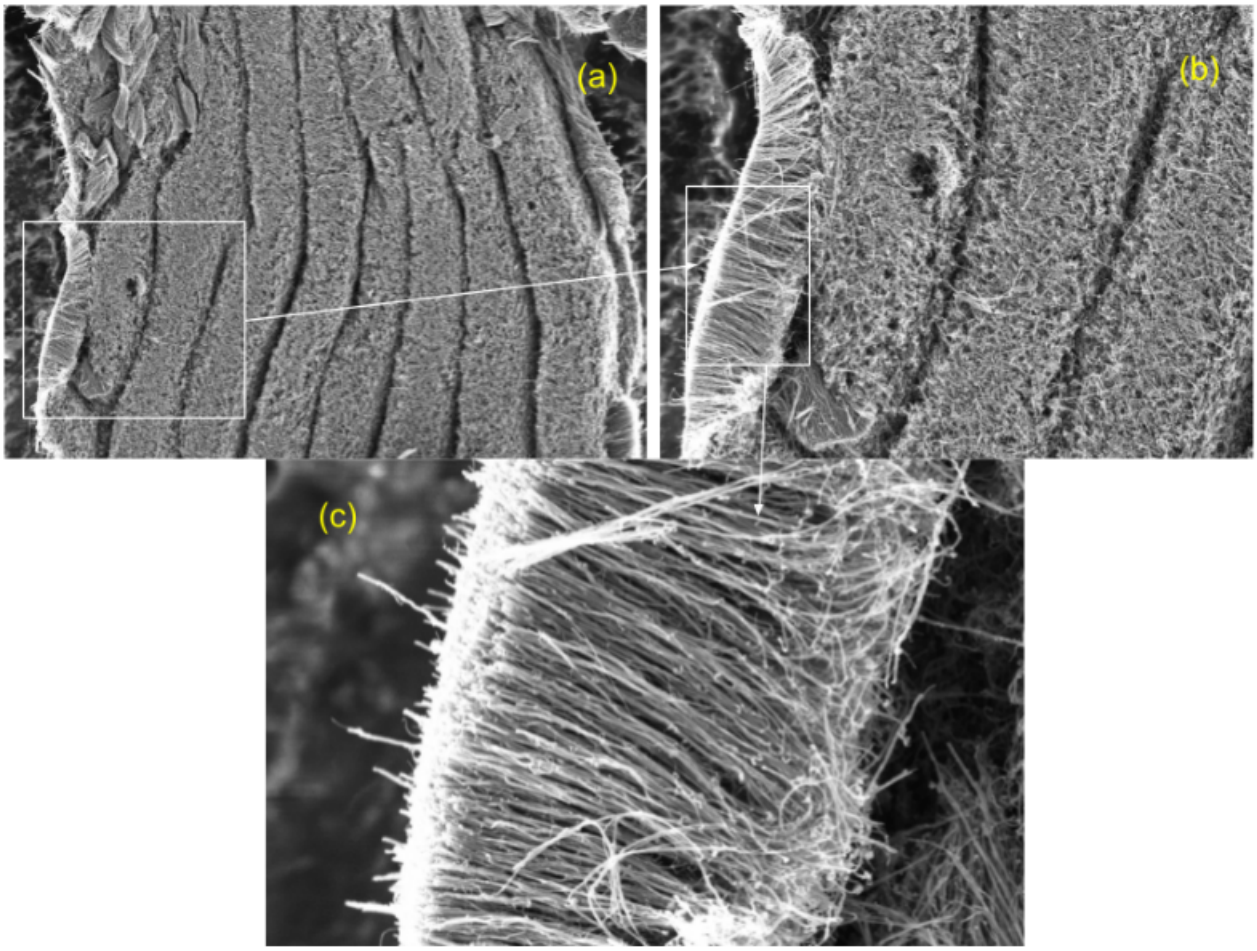

Figure 3.3: FESEM micro-graphs of Fe@CNT. (a) Carpets of aligned forest. (b) Magnified picture of a single carpet of CNTs. (c) Well aligned CNTs

We can see from 3.4 that there are beds of well formed CNTs in alligned-forest morphology. The CNTs of best grade from the constant temperature zone are 10μm in length and 50 nm in diameter. The inner core of iron filling is around 10-15 nm in diameter. As we move away from the centre of the furnace, that is move away from the constant temperature zone, the quality of CNTs formed deteriorates. The CNTs becomes less alligned and more particulate matter is present in the CNTs collected away from the constant temperature zone.

3.2.3 HRTEM on Fe@CNT

HRTEM uses high power electron beams to visualise the structure of the sample. HRTEM can visualize samples upto 100000x magnification. This enables us to visualise the Fe encapsulation much better when compared to FESEM images. The contrast between the Fe encapsulate and the graphitic shells of CNTs are well distinguished. We can also see

that the filling efficiency in the CNTs are also good.

Sample Preparation for HRTEM For TEM imaging, the sample's thickness should be less than 100 nm so that it is thin enough for electrons to penetrate and produce an image. In case of powder samples like CNT, a solution of the sample was made using ethanol as solvent. This is sonicated for 10-15 minutes so that the CNTs get dispersed in the medium. Using a micro-pipette a drop of this dispersed solution is dropped over the TEM grid, which is then dried completely before imaging.

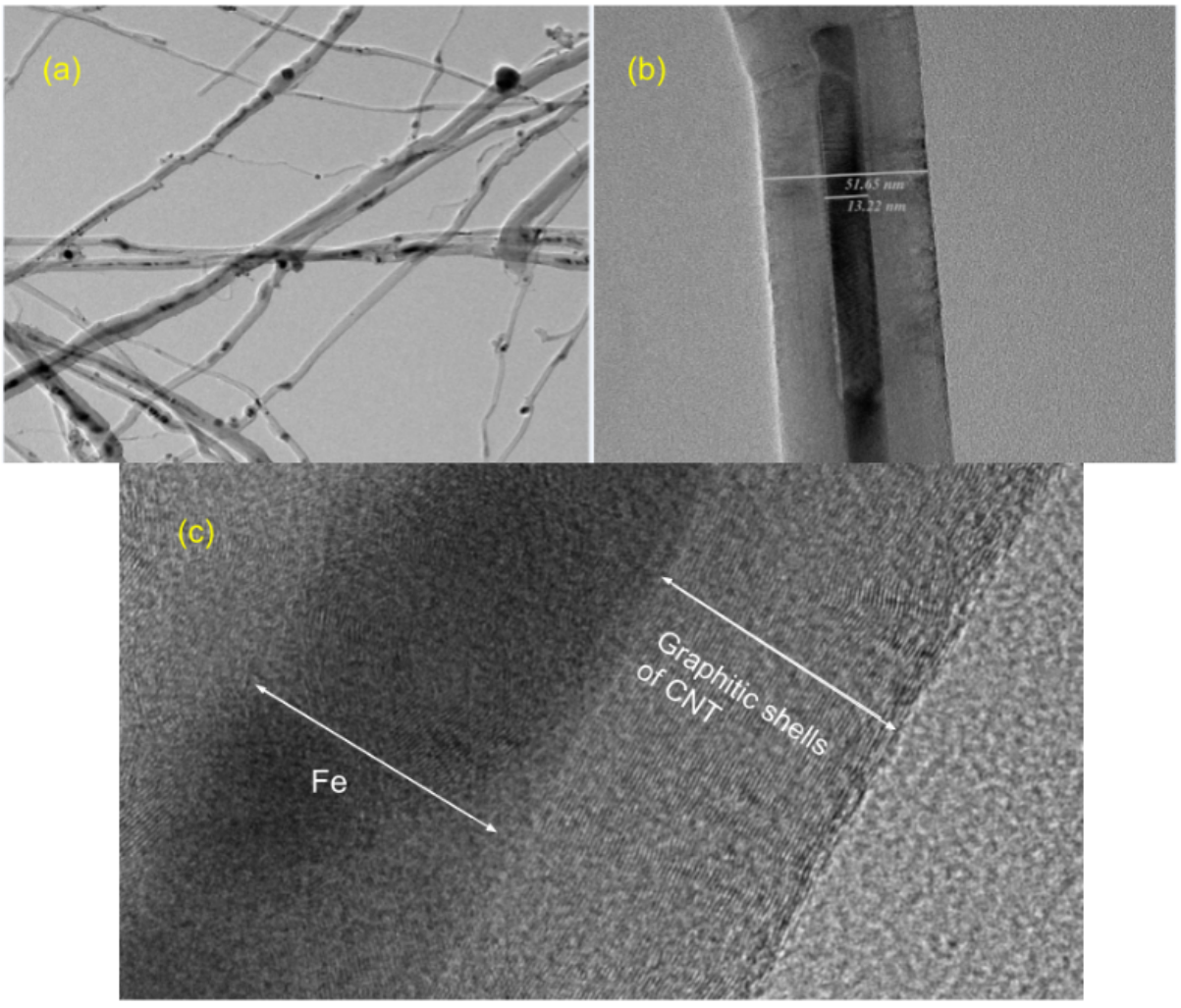

Figure 3.4: HRTEM micro-graphs of Fe@CNT. (a) CNTs encapsulated with Fe particles. (b) Encapsulation of Fe particles inside a CNT. (Please note the diameters of CNT and the Fe filling) (c) TEM micrograph showing the graphitic shells of the MWCNT

3.3 Synthesis and Characterization of Fe_3O_4@CNT pressed pellet

Controlled Oxidation of Fe@CNT in CO_2 environment produces Fe_3O_4@CNT. The synthesis chamber is same as CVD setup for synthesizing Fe@CNTs except, for the absence of the inner quartz tube. Fe@CNTs were scaled up and a pressed pellet of 8 mm diameter and 2 mm thickness was made using them. The synthesis chamber is flushed with CO_2 gas and the furnace is heated upto 500^{o}C. Then the sample boat with Fe@CNT pellet is pushed all the way in such that the sample is placed well inside the constant temperature zone. The pellet was allowed to get oxidised in the CO_2 environment at 500^{o}C for required time. After that, the furnace is switched off and the sample boat is pulled out of the furnace and spot in the chamber which lies around the room temperature. The oxidised pellet is allowed to cool down with CO_2 gas flow.
In A. Kapoor's et. al.'s work, the oxidation of Fe@CNTs was carried out in CO_2 environment to produce α-Fe_2O_3. But there, the Fe@CNTs were placed inside the furnace at room temperature and heated up to the desired temperature under CO_2 gas flow and is left to oxidise at it for an intended time. And then, the sample is left to cool down to room temperature under CO_2 flow inside the furnace. Following this procedure, Dr. A. Kapoor had produced α-Fe_2O_3@CNTs.
Two pellets were oxidised under CO_2 environment as follows

1. Pellet P1 was oxidised at 500^{o}C for 30 min
2. Pellet P2 was oxidised at 500^{o}C for 10 min

3.3.1 Raman Spectroscopy on Fe_3O_4@CNT

The Raman spectrum of Fe_3O_4@CNT reveals prominent peaks at three distinct positions, specifically around 215 cm^{-1}, 278 cm^{-1}, and 393 cm^{-1}, and two fainter bands at 482 cm^{-1} and 595 cm^{-1} in the range below 1000cm^{-1}. Within this spectrum, the peaks detected at 281 cm^{-1} and 399 cm^{-1} are associated with the stretching (Fe–O) mode occurring between two Fe and O atoms. [41] This finding is consistent with previously reported data on Fe_3O_4, confirming the characteristic bands' peak positions.

Above 1000cm^{-1} we can observe the three characteristic Raman peaks for pristine mutliwalled carbon nanotubes around 1350 cm^{-1}, 1583 cm^{-1} and 2692 cm^{-1} which corresponds to the D, G and G' bands respectivelt. This confirms that the Fe@CNT was successfully converted to Fe_3O_4@CNT. The spectra doesn't conatain any others peaks of bands in Raman spectra, thus Fe has got oxidised to Fe_3O_4. Fe_3O_4 has a characterisitic peak around 1250 cm^{-1}. [3, 36, 41, 48]

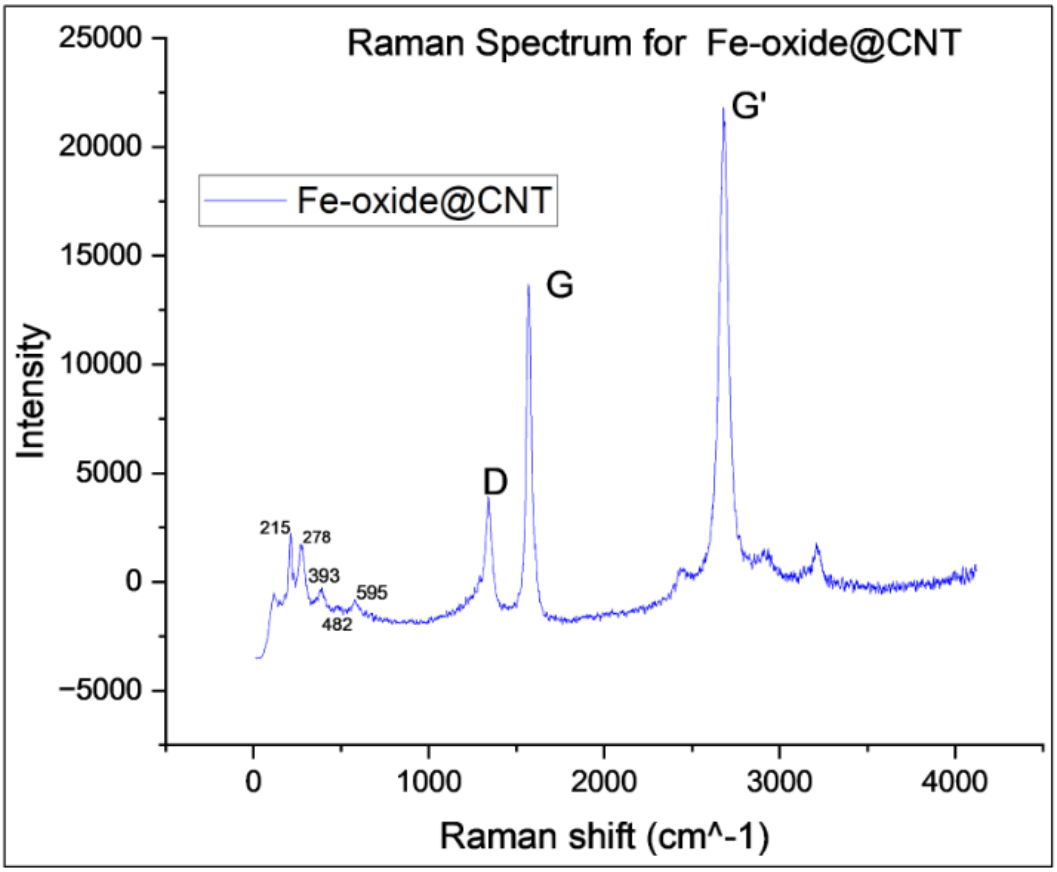

Figure 3.5: Raman Spectrum for Fe@CNT containing Characteristic peaks of both α-Fe_2O_3 and CNTs

3.3.2 Rietveld Refinement of Fe_3O_4@CNT

Rietveld refinement was done using the *FullProf* software. CIF file for graphitic shells was added first for refinement, since the highest fraction of the sample is of CNTs as it was evident from SEM images. After refining for scale factor, zero point of detector, background parameter and instrumental parameters, refinement of lattice parameters, atomic positions, peak shape parameters (U, V, W) was carried out.

From the fractional percentage of composition of each phase obtained after the Reitveld refinement process from Fig 3.6 & 3.7 , we can see that the percentage of Fe_3O_4 is much more than α-Fe in P1 compared to P2. This difference is solely due to the increased time for oxidation in P1 compared to P2. P1 was oxidised for 30 minutes in the CO_2 environment, but P2 was only oxidised for 10 minutes. So in the pellet P1, more amount of Fe could get converted to Fe_3O_4, whereas in P2, there is still a high percentage of unoxidised α-Fe present.

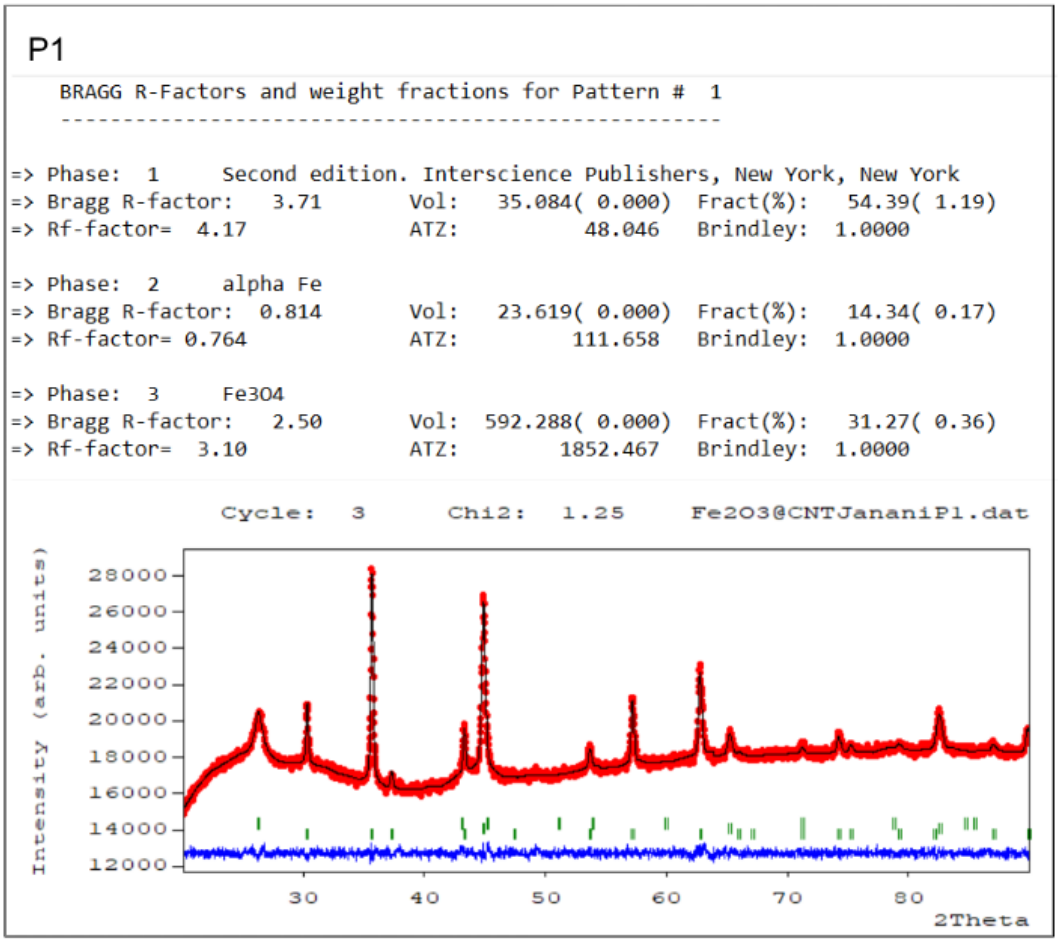

Figure 3.6: Fraction percentage of Fe_3O_4, CNTs(Graphitic shells) and unreacted Fe in Pellet P1. Below is the Rietveld Refinement of the same compound with a very good χ^2 value.

Both the refinements of P1 and P2 have very low χ^2 value of 1.25 and 2.57 respectively, which is an indication for goodness of fit for the refinement. Since all the peaks are well fitted using the C, Fe and Fe_3O_4 we can say that there was no presence of any additional impurity peaks in the sample.

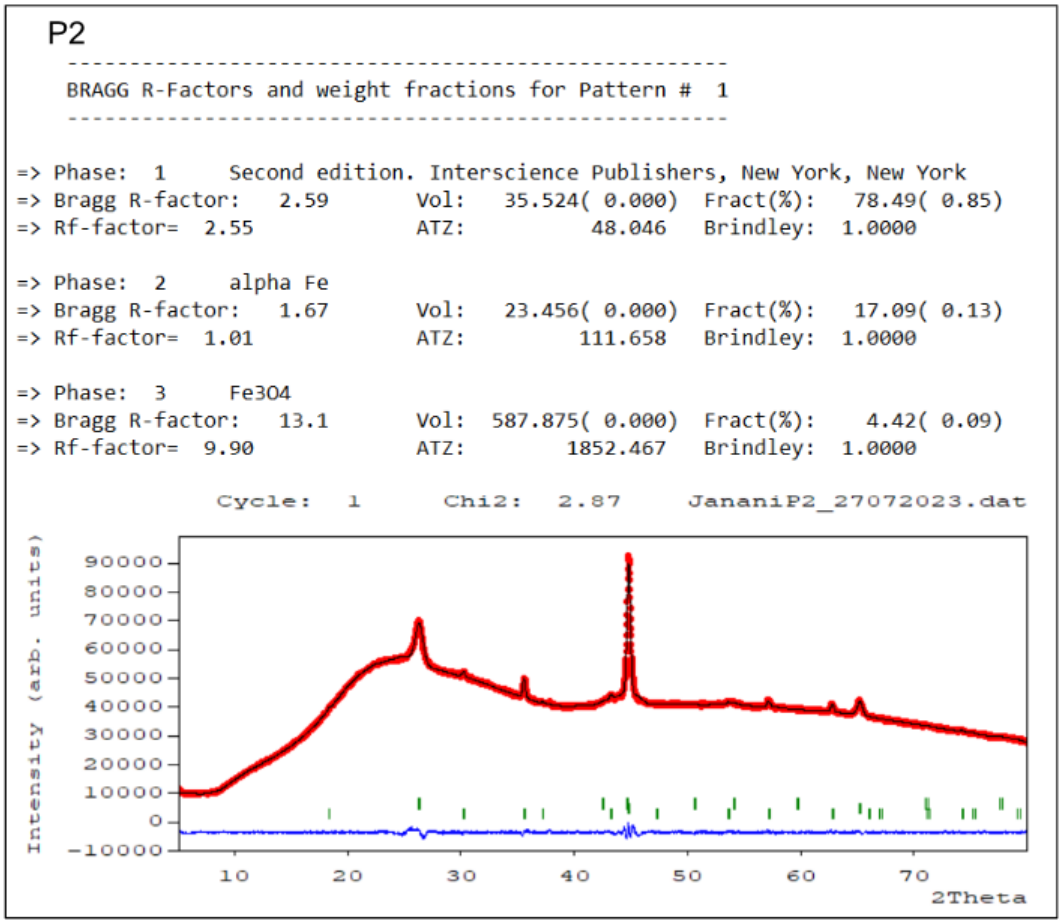

Figure 3.7: Fraction percentage of Fe_3O_4, CNTs(Graphitic shells) and unreacted Fe in Pellet P2. Below is the Rietveld Refinement of the same compound with a very good χ^2 value.

Both the refinements of P1 and P2 have very low χ^2 value of 1.25 and 2.57 respectively, which is an indication for goodness of fit for the refinement. This also ensures that no other phases are present in the compound.

Lattice parameter (a)	**Fe**	**Fe_3O_4**
Literature	2.8608	8.3965
P1	2.86915	8.39803
P2	2.86253	8.377124

Table 3.2: Lattice parameters of Fe and Fe_3O_4 cubic structure obtained after refinement

Graphite	a	b	c
Literature	2.456	2.456	6.696
P1	2.4353	2.4353	6.8311
P2	2.459	2.459	6.7836

Table 3.3: Lattice parameters of Graphite obtained after refinement

Looking at the lattice parameters of Fe_3O_4@CNT, there is some evidence of strain effects in the lattice after encapsulation. However further studies on more samples are needed to confirm the strain effects. Since the mass fraction of Fe_3O_4 is 31.27% in P1 but in P2 it is only 4.42%, we selected sample P1 to do the further measurements. P1 also has lesser fraction of α-Fe particles content.

Chapter 4

Electrical Transport in Fe_3O_4@CNTs

Here we report transport in the pressed pellet of Fe3O4@CNT (Pellet P1). This sample contains Fe_3O_4@CNT (85.66 %) and residual α-Fe particles (14.34 %) outside CNT. We have conducted transport measurements in the temperature range of 5K to 300 K using Closed Cycle Refrigerator when Fe_3O_4 is encapsulated inside CNT. In the following, we first discuss about the intrinsic Verway transition that is known to be present in in Fe_3O_4 before presenting our transport data on Fe_3O_4@CNT.

4.1 Verway Transition

The Verwey transition denotes a phase transition occurring in the mineral magnetite, resulting in modifications to its magnetic, electrical, and thermal properties. Typically, this transition happens at around 120 K. As the temperature increases past the Verwey transition point (T_V), magnetite's crystal lattice undergoes a transformation from a monoclinic insulating structure to a stable metallic cubic inverse spinel arrangement. This phenomenon is named after Evert Verwey, who was the first to establish a connection between this structural shift and the alterations in magnetite's physical characteristics. It marked the groundbreaking discovery of the initial metal-insulator transition. Magnetite (Fe_3O_4) is a cubic inverse spinel compound in which iron cations are situated within the open spaces of a face-centred-cubic (fcc) arrangement of oxygen ions. Within this structure, tetrahedral sites are occupied by Fe^{3+} ions, and octahedral sites are shared by Fe^{3+} and Fe^{2+} ions. The presence of both Fe^{3+} and Fe^{2+} ions in the octahedral sites results in relatively low electrical resistivity at room temperature, primarily due to the movement of charge carriers between Fe^{3+} and Fe^{2+} ions.[6] In case of Fe_3O_4, as the temperature decreases, there is a significant increase in resistivity by about two to three orders of magnitude at $\sim$120K. This transformation is referred to as the "Verwey transition." It is attributed to the reorganization of charges among Fe^{3+} and Fe^{2+} ions occurring below

the Verwey transition temperature. [6, 19]

The Verwey transition temperature and its manifestation in physical properties are strongly influenced by size effects in Fe_3O_4. It also changes with the stress applied to magnetite and its chemical composition. Introducing non-stoichiometry through processes such as substituting metal cations or partial oxidation has the potential to decrease the transition temperature or even completely prevent it. [25, 52]

It is clear from Fig. 4.1 that the Verway transition is most distinctly visible in the case of bulk crystal measurements of ρ vs. T. For the crystal, there is a discontinuity around its T_V (∼120K) with resistivity increase of about three orders of magnitude. For the thin-film with thickness of 200 nm, T_V is lower and the Verway transition becomes broader (there is no discontinuity). The resistivity increases by about two orders of magnitude around its T_V. For thin-film with a thickness of 50 nm, the transition is even broader and T_V is even lower. Resistivity increases by less than two orders of magnitude around its T_V. Whereas for thin-film with a thickness of 15 nm, ρ vs. T graph has a very smooth curve, with no abrupt change in the curve. Change in the magnitude of resistivity from 300K to 60K for the crystal and thin-film of thickness 200 and 50 nm was about 3–4 orders of magnitude, whereas for the 15 nm thin-film, it was only 2 orders of magnitude. [38, 62]

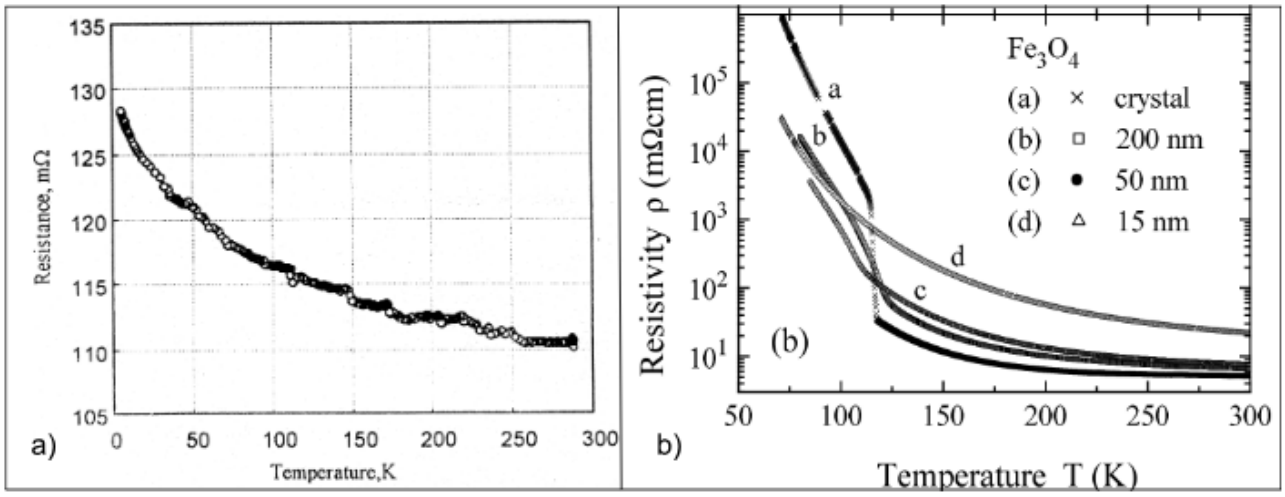

Figure 4.1: a) Resistance vs. Temperature graph for hot-pressed MWCNTs. (Taken from [38]) b) Resistivity vs. Temperature graph for Fe_3O_4 in bulk (crystal) and thin films of various thickness. (Taken from [62])

In literature, the size effects on the Verway transition in the Fe_3O_4 nanoparticles are reported. But we are interested in exploring the interface effects on the Verway transition when Fe_3O_4 is encapsulated inside CNTs. In the case of pristine multi-walled CNTs, they

can exhibit semi-conducting or metallic conduction behaviour [**WangYaZhou**, 38, 56] however resistance of hot-pressed pellet of CNTs shows a semi-conductor like R vs. T curve but has a much lower value of resistance. [38]

4.2 Temperature variaiton of resistance on Fe_3O_4@CNTs

4.2.1 Setup for Resistance Measurements

A Printed Circuit Board (PCB) with printed Gold contacts was used for the measurements. The pellet was used like a pencil to gently write over the PCB to make a connection between two gold contacts. This creates a clean layered structure of Fe_3O_4@CNTs between the contacts. The layered CNTs forms an electrical path which connects the gold contacts and thus allows for electrical conductivity between them.

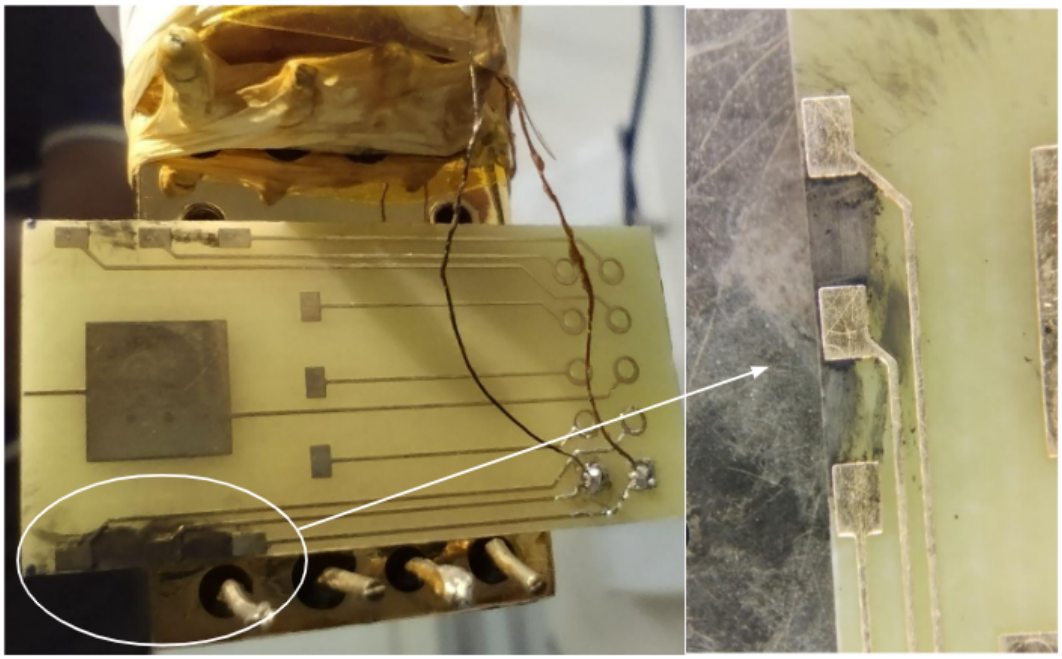

Figure 4.2: A PCB with with Gold contacts connected written over it using Fe_3O_4@CNTs.

The CNTs make up a continuous layer between the contacts which can be seen from images 4.2 and 4.3.

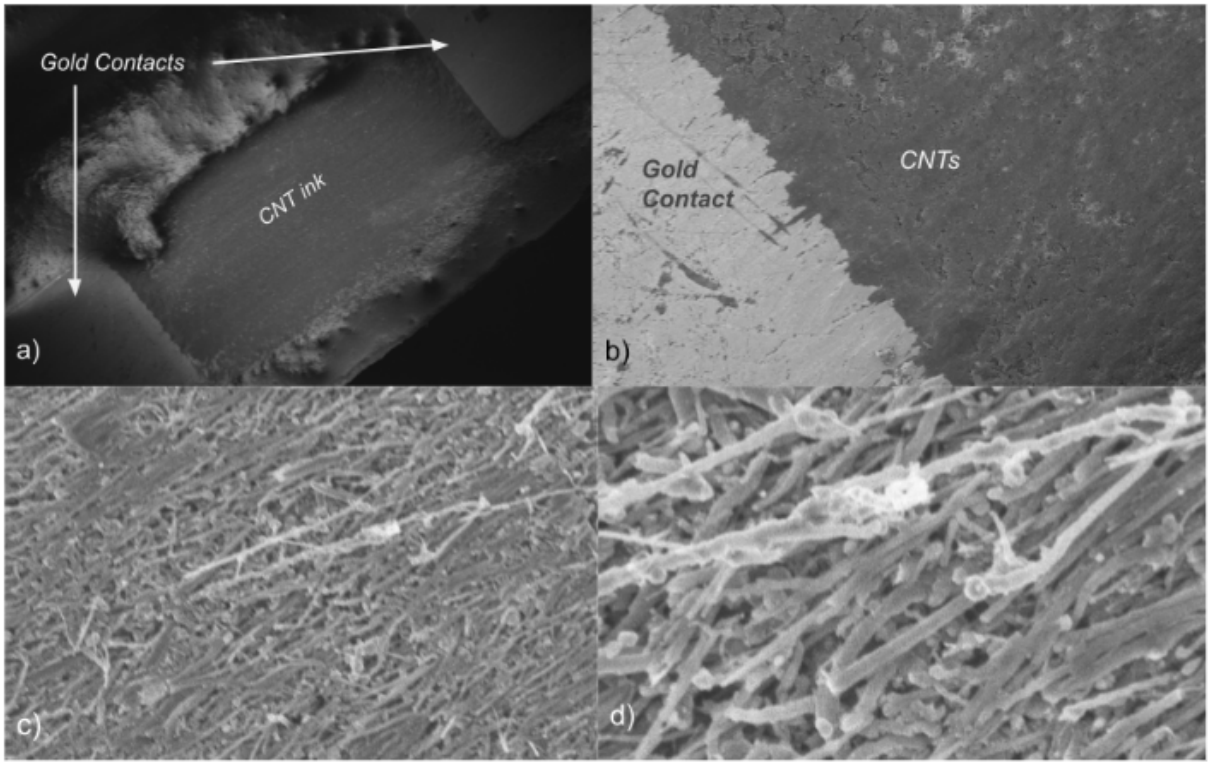

Figure 4.3: (a) & (b) Closer SEM image of the CNT ink connection between gold contacts. (c) & (d) SEM image of continuous layer of Fe_3O_4@CNTs over the PCB.

4.2.2 Resistance Measurements and Verway Transition

Fe_3O_4 undergoes a transition from metallic inverse spinel structure to a monoclinic insulator structure when cooled down below its T_V. This is observed from a temperature variation of resistivity plot as the resistivity increases by 3 to 4 orders of magnitude from room temperature to a temperature well below T_V. Even in thin films with a thickness of 85nm, this transition is well observed as the resistivity increases by 3 to 4 orders of magnitude. [33]

X. W. Li and colleagues have demonstrated that in Fe_3O_4 thin films of varying thickness, the change in resistance during the transition becomes less pronounced, and the transition becomes broader as the film thickness decreases. Moreover, for the thinnest films, the transition is hardly noticeable. On the other hand, Ozden and their team's work indicates that the Verwey transition occurs in magnetite crystals with near-stoichiometric composition for all sizes above 37 nm. Below this size threshold, the effects of superparamagnetism become prominent, making it challenging to detect T_v (the Verwey transition temperature). They have also found that even slight deviations from stoichiometry in magnetite significantly impact the Verwey transition. This influence is vividly demon-

strated by the broadening and eventual suppression of the transition in partially oxidized magnetite samples. [33, 44]

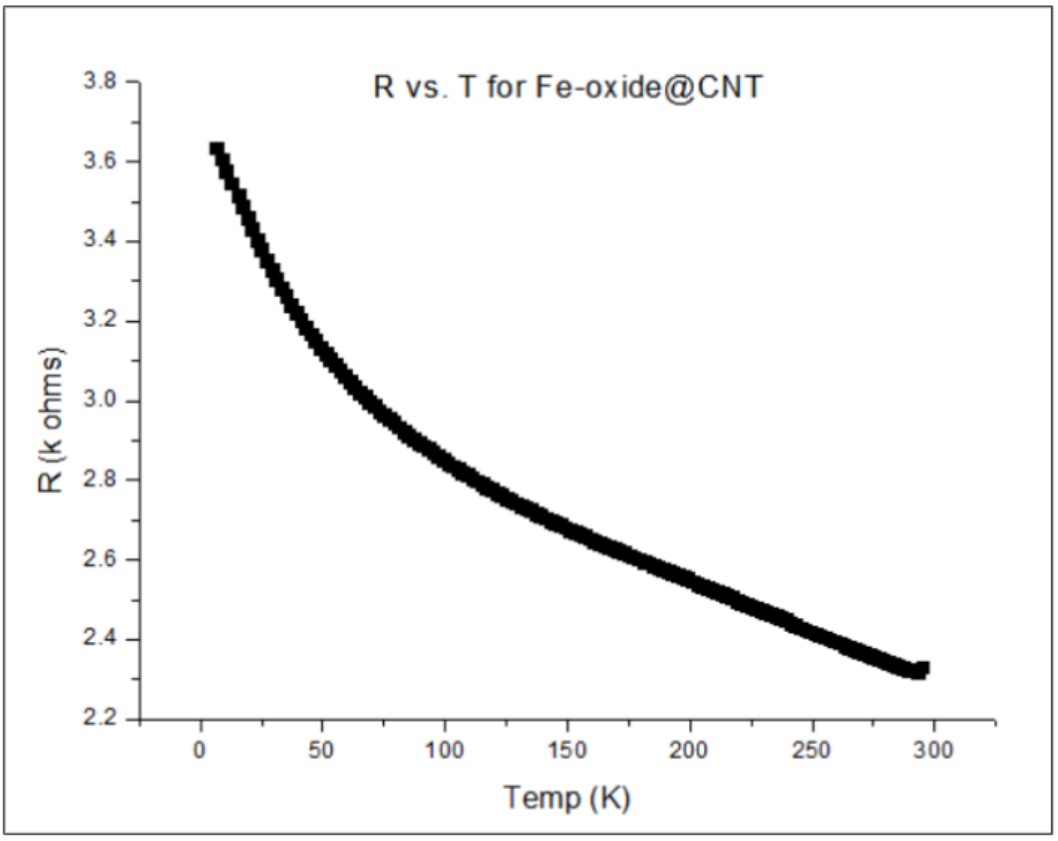

Figure 4.4: Resistance vs. Temperature graph of P1 CNT ink on PCB. (2-probe)

From the temperature variation of resistance of Fe_3O_4@CNT 4.4 we observe that the funtional form is semi-conducting like. However the resistance at 5K is about 1.5 times of its value at 300 K. Also the signatures of Verway transition through the interface effects are not observable. If whether the Verway transition has moved to a lower temperatures due to the size of the encapsulate (which can be upto 15nm in diameter and few 100 nm in length) could not be confirmed from the existing data. Temperature variation of XRD especially in the lower temperature range can be used to probe the structural transition associated with the Verway transition. This may help in identifying the existence of interface effects in transport measurements. This is especially relevant as interface effectsin magnetisation measurements have been observed previously in Fe_2O_3@CNT in the vicinity of Morin transition. [29]

Functional form of the R vs. T in Fe_3O_4@CNT was investigated by fitting Variable Range Hopping mdel which is presented in the next sub-section.

4.3 Variable-Range Hopping (VRH) Mechanism of Conduction in CNTs

This model of conduction describes the low temperature conduction in a strongly disordered system with localized states. This model was proposed by Mott. According to his theory, the electrical conduction does not obey the classical process of diffusion but follows a variable-range hopping (VRH). Here, electrons hop from one initial site to another with an energy of hop as low as possible. For such energy, the second site is statistically located far from the first, involving a distance which is larger than the decay length of the wave function. Mott first pointed out that at low temperatures the most frequent hopping would not be to the nearest neighbour. Mott's Variable Range Hopping model gives the relation between conductivity and temperature T:

$$\sigma(T) = \sigma_o \exp\{-(T_o/T)^{\alpha}\} \tag{4.1}$$

Where $\alpha = 1/(1+d)$ and d is the dimensionality.

Thus the relation between the resistance (R) and the temperature (T)is given by:

$$R(T) = R_o \exp\{(T_o/T)^{\alpha}\} \tag{4.2}$$

Taking the natural log on both sides and accounting for the dimensionality, we get the following relations:

$$Ln(R) \propto T^{-\alpha} \quad \Rightarrow \quad \begin{aligned} &1D : Ln(R) \propto T^{-\frac{1}{2}} \\ &2D : Ln(R) \propto T^{-\frac{1}{3}} \\ &3D : Ln(R) \propto T^{-\frac{1}{4}} \end{aligned}$$

Plotting the graph for Ln(R) vs T^{α} for 1D, 2D and 3D, we get the following graphs:

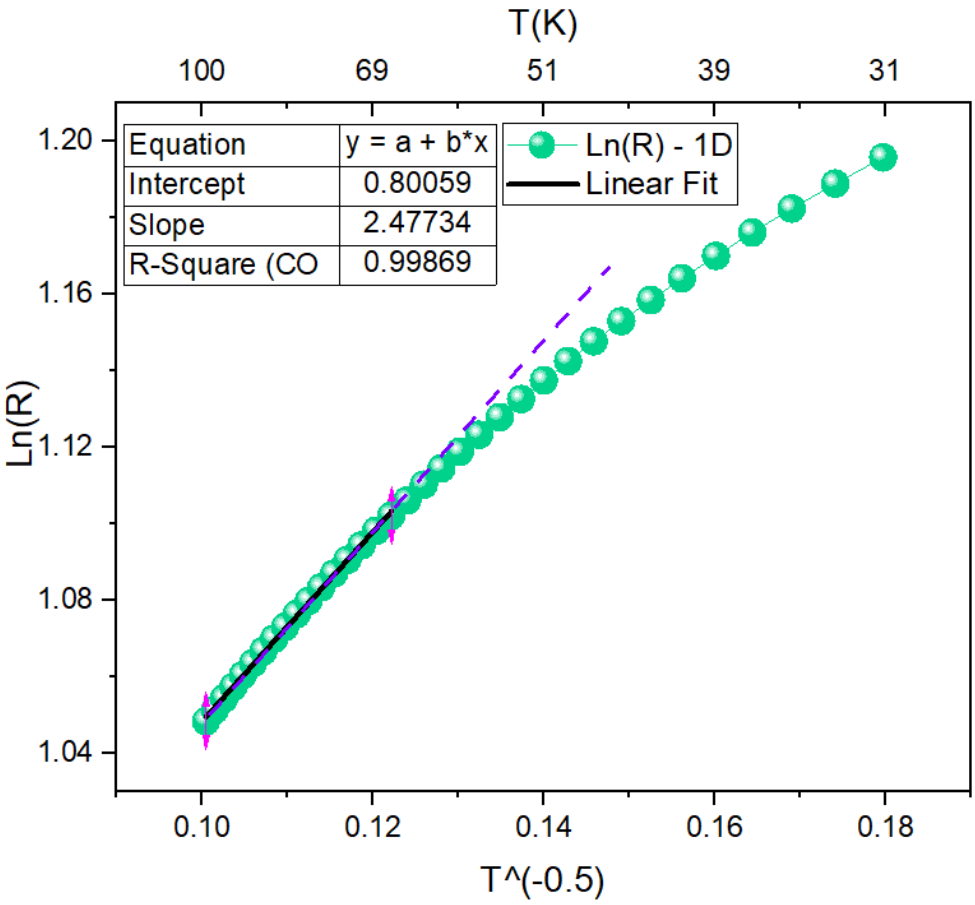

Figure 4.5: Ln(R) vs $T^{(-0.5)}$. VRH for 1D

We can see that the VRH model for 1D can be only fitted for the temperature range of 70 K < T < 100 K. Below 70K, the graph deviates significantly from linearity.

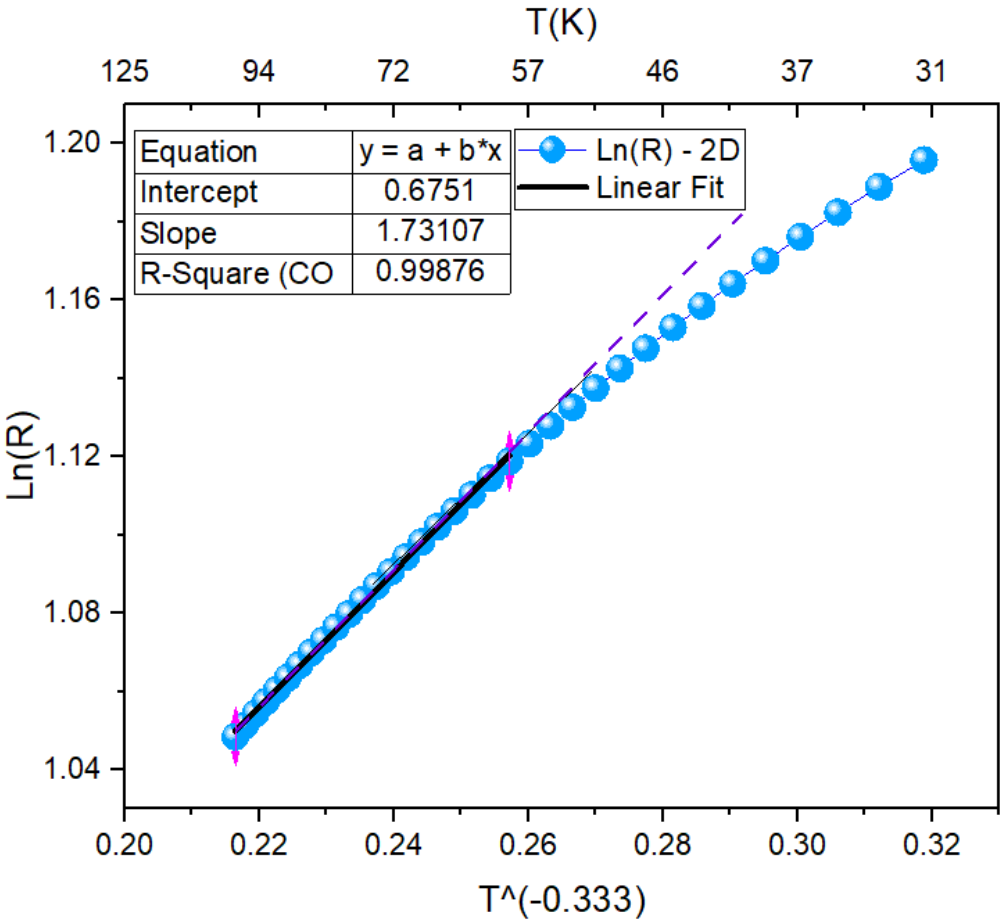

Figure 4.6: Ln(R) vs $T^{(-0.333)}$. VRH for 2D

The VRH model for 2D gave us a better fit when compared to the 1D model. This model was able to be fit for the temperature range of 60 < T < 100 K. Below 60 K, the data deviates from linearity, and the VRH model for 2D doesn't explain the behaviour for an extended range.

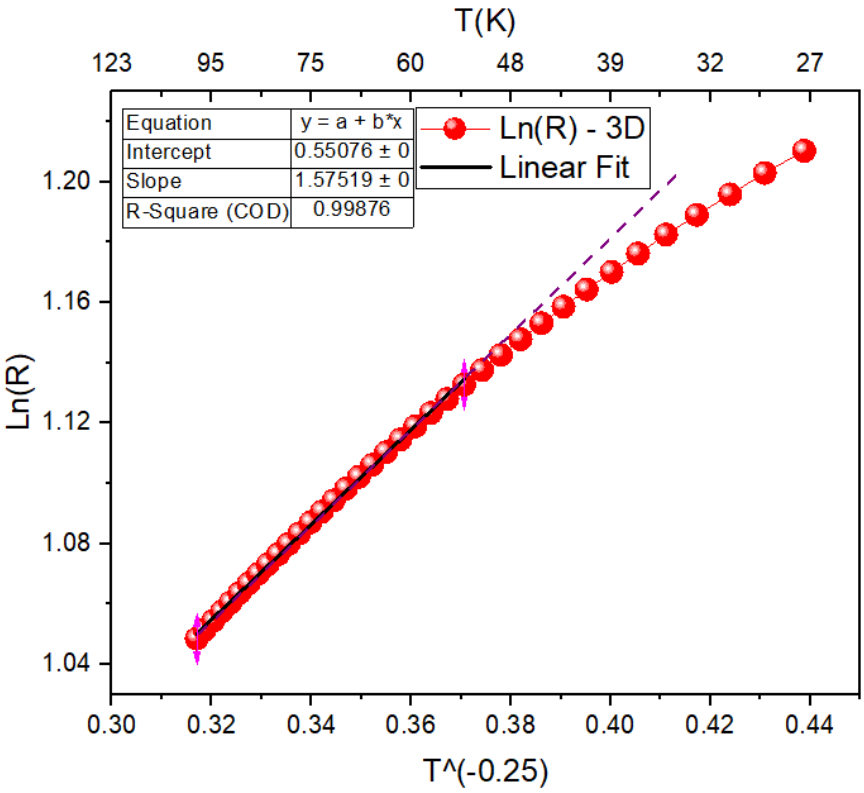

Figure 4.7: Ln(R) vs $T^{(-0.25)}$. VRH for 3D

The VRH model for 3D was an even better fit. This model was able to be fit for the temperature range of 54 < T < 100 K. Below 54 K, the data deviates from linearity, and the VRH model for 3D doesn't explain the behaviour for an extended range. But for a limited range at low temperatures, the VRH model for 3D explains the behaviour of resistance to an extent.

We should note that there is a possibility that the Verway transition might still happen, but the transition might have shifted towards the lower temperature and also might happen in a broad temperature range. This might be the reason, why the R vs. T graph is deviating from linearity below 54 K for Ln(R) vs. $T^{-0.25}$.

Thus, further studies like magneto-resistance measurements and temperature variation XRD can reveal more insights about the structural changes in Fe_3O_4@CNTs and possibly also the strain effects arising in the material due to the encapsulation of Fe_3O_4 into the CNTs.

Chapter 5

Conclusions and Future Work

The most well-known ferrimagnetic material, Fe_3O_4 was successfully encapsulated inside Carbon Nanotubes (CNTs) to produce Fe_3O_4@CNTs. Encapsulation of Fe_3O_4 inside carbon nanotubes (CNTs) i.e Fe_3O_4@CNT has many possible applications in spintronic devices, ferrofluids, magnetic coatings, etc. Magnetite has a metallic cubic inverse-spinel structure at room temperature and a high Curie temperature of 858K. It also possesses a low-temperature phase transition, the Verway transition, which happens around 120K below which it becomes an insulator with a monoclinic structure. Verway transition is associated with changes in its magnetic, electrical, and thermal properties. Metallocens are highly studied precursor material for the synthesis of multi-walled CNTs (MWCNTs) with metal filling. So, ferrocene was chosen as the precursor for synthesising CNTs.

The Chemical Vapour Deposition (CVD) method was used for the synthesising the CNTs. Here, The Nabertherm R 100/750/13 Single-zone Furnace for Solid-state CVD of ferrocene to produce CNTs, instead of the conventional Dual-zone furnace. The furnace has a constant temperature region in the middle, which can hold the temperature we set with a very high accuracy. Towards both the outer edges, the furnace has a variable temperature region. Temperature profiling of the variable temperature region was performed on the furnace at the pyrolysis temperature (T_{pyro}). The required sublimation temperature (T_{sub}) was 300^oC. A temperature profile was used to determine the spot inside the furnace to which the sample boat had to be pushed inside to remain at 300^oC.

From Dr. Kapoor et. al.'s work, we we used the optimised values of T_{sub} as 300^oC and T_{pyro} as 900^oC in order to produce Fe@CNTs in aligned forest morphology. Once the Fe@CNT sample was formed, it was characterized using techniques like XRD, FESEM, HR-TEM, Raman spectroscopy etc. The Fe@CNTs had well-formed graphitic shells with iron filling inside the CNTs. The quality of the CNTs depended on the region it was formed inside the furnace. Rietveld analysis of XRD was done to confirm that there are no impurity peaks in the sample. Subsequently, the same procedure was followed in order

to scale up the amount of Fe@CNTs to proceed further.

According to Dr. Kapoor et. al.'s work, 500mg of ferrocene was used to prepare Fe@CNTs in one run. This produced around ∼55mg of best quality and ∼90mg of second best quality CNTs. However, increasing the precursor amount to 700 mg nearly doubled the yield of fe@CNTs. In this case, ∼120mg of best quality and ∼180mg of second best quality CNTs were produced. This greatly helped in the scaling-up process.

The same furnace without the inner tube was used for the oxidation of Fe@CNTs. Fe@CNTs were made into a pellet of 2mm thickness and 8 mm in diameter. The furnace is set to be heated up to 500^oC under CO_2 flow, where the pellet is placed on the sample boat such that it remains at room temperature. Once the furnace was stabilized at 500^oC, the sample boat was pushed to the constant temperature zone. The pellet is left to oxidise for the desired time and the sample boat is pulled back such that it comes to room temperature immediately. Note that the pellet wasn't inside the furnace as it cooled down to room temperature. Dr A. Kapoor et. al. tried a similar oxidation procedure of Fe@CNTs powder in a CO_2 environment to produce α-Fe_2O_3@CNTs. But there, the Fe@CNTs were placed inside the furnace (at a constant temperature zone) at room temperature, heated up to 500^oC under CO2 gas flow, and left to oxidise at that temperature for an intended time. Then, the sample was let cool down to room temperature under CO_2 flow inside the furnace (at a constant temperature zone).

While Fe@CNT and FeO_x@CNT have been synthesized previously in our lab using the single zone furnace, this work brings forward the issue of yield. where by increasing the precursor amount by 40% the yield was almost doubled. The heating procedure during the conversion of Fe@CNT in CO_2 environment is very particular to the formation Fe_3O_4@CNTs without any other oxides of Iorn. Since multiple oxides of iron are formed in the close vicinity, the exact temperature, time of annealing and the way the sample is cooled down after oxidation is important.
Rietveld refinement of Fe_3O_4@CNTs was carried out and phases of graphite, Fe_3O_4 and α-Fe were used for structural refinement. There was no presence of any impurity peaks, and the peaks were well-fitted using the above-mentioned phases. This analysis helped us to know that increasing the oxidation time results in more amount of α-Fe getting converted into Fe_3O_4 in the CNTs.

This pellet was used like a pencil to write between the two gold contacts of a printed circuit board (PCB) to make a clean electrical path. SEM images of this PCB connection show that the CNT ink forms a continuous layer between the gold contacts. This PCB was attached to a CCR setup for a 2-probe temperature variation resistance measure-

ment. The room-temperature resistance of the connection was around 2.3 kΩ. Which is around three orders of magnitude more than the resistance of MWCNTs and Fe_3O_4 thin films.

The Verway transition was also not observed in Fe_3O_4@CNTs. This could be due to a number of reasons like the small size of the Fe_3O_4 particles inside CNTs, the stochiometry of the Fe_3O_4 formed inside the CNTs, the effect of unoxidised α-Fe present in the CNTs, and also the possible interface effects arising from the encapsulation of Fe_3O_4 inside the CNTs.

The Variable-range Hopping (VRH) model for 3D was able to be fit for the temperature range of $54 < T < 100$ K. Below 54 K, the data deviates from linearity, and the VRH model for 3D doesn't explain the behaviour for an extended range. But for a limited range at low temperatures, the VRH model for 3D explains the behaviour of resistance to an extent.The Verway transition might still happen, but the transition might have shifted towards the lower temperature and also might happen in a broad temperature range. This might be the reason why the R vs. T graph is deviating from linearity below 54 K for Ln(R) vs. $T^{-0.25}$.

Thus, further studies like magneto-resistance measurements and temperature variation XRD can reveal more insights about the structural changes in Fe_3O_4@CNTs and possibly also the strain effects arising in the material due to the encapsulation of Fe_3O_4 into the CNTs. It will be interesting to perform magnetoresistance measurements on the existing samples . These measurements will reveal if magnetic state of the encapsulate impacts the transport properties through the strain effects at the interface. In addition, it would also be interesting to enhance the length of the encapsulate (the oxide) within the CNT, so as to form longer Fe_3O_4 nanowires inside CNT. This may lead to the observation of Verwey transition in the oxide nanowires through magnetic measurements. Further studies on the sample need to be done to understand whether there is a structural change in Fe_3O_4 when it is cooled down to a low temperature. Temperature variation XRD analysis would be able to provide a better view regarding this. Various other measurements, like magneto-resistance or magnetic susceptibility measurements, can also be done to understand the magnetic behaviour of Fe_3O_4@CNTs.

Bibliography

[1] R. Andrews et al. "Continuous production of aligned carbon nanotubes: a step closer to commercial realization". In: *Chemical Physics Letters* 303.5 (1999), pp. 467–474. ISSN: 0009-2614. DOI: https://doi.org/10.1016/S0009-2614(99)00282-1.

[2] A Bajpai et al. "A carbon-nanotube based nano-furnace for in-situ restructuring of a magnetoelectric oxide". In: *Carbon* 114 (Apr. 2017). © 2016 Elsevier Ltd. This is an author produced version of a paper published in Carbon. Uploaded in accordance with the publisher's self-archiving policy., pp. 291–300.

[3] Nagaraj Basavegowda, Kanchan Mishra, and Yong Rok Lee. "Synthesis, characterization, and catalytic applications of hematite (α-Fe2O3) nanoparticles as reusable nanocatalyst". In: *Advances in Natural Sciences: Nanoscience and Nanotechnology* 8.2 (2017), p. 025017.

[4] Alberto Bianco, Kostas Kostarelos, and Maurizio Prato. "Applications of carbon nanotubes in drug delivery". In: *Current Opinion in Chemical Biology* 9.6 (2005). Biopolymers / Model systems, pp. 674–679. ISSN: 1367-5931. DOI: https://doi.org/10.1016/j.cbpa.2005.10.005.

[5] Stephen Blundell. "Magnetism in Condensed Matter". In: *American Journal of Physics* 71.1 (2003), pp. 94–95. DOI: 10.1119/1.1522704. eprint: https://doi.org/10.1119/1.1522704.

[6] John Bowles. "The Iron Oxides: Structure, Properties Reactions Occurrence and Uses (Review)". In: *Mineralogical Magazine - MINER MAG* 61 (Oct. 1997), pp. 740–741. DOI: 10.1180/minmag.1997.061.408.20.

[7] James Howe Brent Fultz. "Transmission Electron Microscopy and Diffractometry of Materials". In: *Transmission Electron Microscopy and Diffractometry of Materials*. Vol. 4. Springer Berlin, Heidelberg, 2012, p. 764. DOI: https://doi.org/10.1007/978-3-642-29761-8.

[8] Andres Cantarero. "Raman Scattering Applied to Materials Science". In: *Procedia Materials Science* 9 (Dec. 2015). DOI: 10.1016/j.mspro.2015.04.014.

[9] Philip Collins and Phaedon Avouris. "Nanotubes for Electronics". In: *Scientific American* 283 (Jan. 2001), pp. 62–9. DOI: 10.1038/scientificamerican1200-62.

[10] Ruchita S. Das and Y.K. Agrawal. "Raman spectroscopy: Recent advancements, techniques and applications". In: *Vibrational Spectroscopy* 57.2 (2011), pp. 163–176. ISSN: 0924-2031. DOI: https://doi.org/10.1016/j.vibspec.2011.08.003.

[11] L.M. Dyagileva et al. "Reactivity of the first transition row metallocenes in thermal decomposition reaction". In: *Journal of Organometallic Chemistry* 175.1 (1979), pp. 63–72. ISSN: 0022-328X. DOI: https://doi.org/10.1016/S0022-328X(00)82299-8.

[12] Ali Eatemadi et al. "Carbon nanotubes: Properties, synthesis, purification, and medical applications". In: *Nanoscale research letters* 9 (Aug. 2014), p. 393. DOI: 10.1186/1556-276X-9-393.

[13] Ali Eftekhari, Parvaneh Jafarkhani, and Fathollah Moztarzadeh. "High-yield synthesis of carbon nanotubes using a water-soluble catalyst support in catalytic chemical vapor deposition". In: *Carbon* 44 (June 2006), pp. 1343–1345. DOI: 10.1016/j.carbon.2005.12.006.

[14] T. Filleter et al. "Ultrahigh Strength and Stiffness in Cross-Linked Hierarchical Carbon Nanotube Bundles". In: *Advanced Materials* 23.25 (2011), pp. 2855–2860. DOI: https://doi.org/10.1002/adma.201100547. eprint: https://onlinelibrary.wiley.com/doi/pdf/10.1002/adma.201100547.

[15] John E Fischer and Alan T Johnson. "Electronic properties of carbon nanotubes". English. In: *Current Opinion in Solid State Materials Science* 4.1 (1999), pp. 28–33.

[16] C. Fong, J. Pask, and Lin Yang. *Half-metallic Materials and Their Properties*. May 2013. ISBN: 978-1-908977-12-0.

[17] D. Givord. "Magnetic properties and magnetic order". In: *Encyclopedia of Condensed Matter Physics* (Dec. 2005).

[18] G. Grechnev et al. "Structure and magnetic properties of multi-walled carbon nanotubes modified with iron". In: *Low Temperature Physics* 36 (Dec. 2010), pp. 1086–1090. DOI: 10.1063/1.3530422.

[19] "25 - Iron, Ruthenium and Osmium". In: *Chemistry of the Elements (Second Edition)*. Ed. by N.N. GREENWOOD and A. EARNSHAW. Second Edition. Oxford: Butterworth-Heinemann, 1997, pp. 1070–1112. ISBN: 978-0-7506-3365-9. DOI: https://doi.org/10.1016/B978-0-7506-3365-9.50031-6.

[20] T. Guo et al. "Catalytic growth of single-walled manotubes by laser vaporization". In: *Chemical Physics Letters* 243.1 (1995), pp. 49–54. ISSN: 0009-2614. DOI: https://doi.org/10.1016/0009-2614(95)00825-O.

[21] Christopher Hammond. "The Basics of Crystallography and Diffraction (2nd edn)". In: *Measurement Science and Technology* 13.2 (Feb. 2002), p. 232. DOI: 10.1088/0957-0233/13/2/708.

[22] Silke Hampel et al. "Growth and characterization of filled carbon nanotubes with ferromagnetic properties". In: *Carbon* 44 (Sept. 2006), pp. 2316–2322. DOI: 10.1016/j.carbon.2006.02.015.

[23] James Hone. "Phonons and Thermal Properties of Carbon Nanotubes". In: *Springer Berlin Heidelberg* (2001), pp. 273–286. DOI: 10.1007/3-540-39947-X_11.

[24] John Hone et al. "Thermal Properties of Carbon Nanotubes and Nanotube-Based Materials". In: *Applied Physics A* 74 (Jan. 2002), pp. 339–343. DOI: 10.1007/s003390201277.

[25] R. Itai et al. "Electrical Resistivity of Magnetite Anodes". In: *Journal of The Electrochemical Society* 118.10 (Oct. 1971), p. 1709. DOI: 10.1149/1.2407817.

[26] S. Jain, A. O. Adeyeye, and C. B. Boothroyd. "Electronic properties of half metallic Fe3O4 films". In: *Journal of Applied Physics* 97.9 (Apr. 2005), p. 093713. ISSN: 0021-8979. DOI: 10.1063/1.1889247. eprint: https://pubs.aip.org/aip/jap/article-pdf/doi/10.1063/1.1889247/13114235/093713_1_online.pdf.

[27] AAKANKSHA KAPOOR. "Encapsulation of magnetic oxides inside carbon nanotubes". English. PhD thesis. Indian Institute of Science Education and Research (IISER) Pune, 2020.

[28] Aakanksha Kapoor et al. "3d transition metals and oxides within carbon nanotubes by co-pyrolysis of metallocene camphor: High filling efficiency and self-organized structures". In: *Carbon* 132 (2018), pp. 733–745. ISSN: 0008-6223. DOI: https://doi.org/10.1016/j.carbon.2018.02.092.

[29] Aakanksha Kapoor et al. "Enhanced Magnetism Time - Stable Remanence at the Interface of Hematite and Carbon Nanotubes". In: (Oct. 2018).

[30] Mukul Kumar and Yoshinori Ando. "Chemical Vapor Deposition of Carbon Nanotubes: A Review on Growth Mechanism and Mass Production". In: *Journal of nanoscience and nanotechnology* 10 (June 2010), pp. 3739–58. DOI: 10.1166/jnn.2010.2939.

[31] Mukul Kumar and Yoshinori Ando. "Single-wall and multi-wall carbon nanotubes from camphor - A botanical hydrocarbon". In: *Diamond and Related Materials* 12 (Oct. 2003), pp. 1845–1850. DOI: 10.1016/S0925-9635(03)00217-6.

[32] A. Leonhardt et al. "Synthesis, Properties, and Applications of Ferromagnetic-Filled Carbon Nanotubes". In: *Chemical Vapor Deposition* 12 (June 2006), pp. 380–387. DOI: 10.1002/cvde.200506441.

[33] X. Li et al. “Transport and Magnetic Properties of Epitaxial and Polycrystalline Magnetite Thin Films”. In: *Journal of Applied Physics* 83 (June 1998). DOI: 10.1063/1.367547.

[34] Xuelei Liang et al. “Carbon Nanotube Thin Film Transistors for Flat Panel Display Application”. In: *Topics in Current Chemistry* 374 (Nov. 2016). DOI: 10.1007/s41061-016-0083-6.

[35] Lei Liu et al. “Controllable Reversibility of an sp^2 to sp^3 Transition of a Single Wall Nanotube under the Manipulation of an AFM Tip: A Nanoscale Electromechanical Switch?” In: *Phys. Rev. Lett.* 84 (21 May 2000), pp. 4950–4953. DOI: 10.1103/PhysRevLett.84.4950.

[36] Jie-Feng Lu and Cho-Jen Tsai. “Hydrothermal phase transformation of hematite to magnetite”. In: *Nanoscale research letters* 9 (May 2014), p. 230. DOI: 10.1186/1556-276X-9-230.

[37] Jingshan Luo et al. “Three-Dimensional Graphene Foam Supported Fe3O4 Lithium Battery Anodes with Long Cycle Life and High Rate Capability”. In: *Nano Letters* 13.12 (2013). PMID: 24219630, pp. 6136–6143. DOI: 10.1021/nl403461n. eprint: https://doi.org/10.1021/nl403461n.

[38] R.Z Ma et al. “Electrical conductivity and field emission characteristics of hot-pressed sintered carbon nanotubes”. In: *Materials Research Bulletin* 34.5 (1999), pp. 741–747. ISSN: 0025-5408. DOI: https://doi.org/10.1016/S0025-5408(99)00064-1.

[39] Seyyed Shayan Meysami et al. “Aerosol-assisted chemical vapour deposition synthesis of multi-wall carbon nanotubes: III. Towards upscaling”. In: *Carbon* 88 (Feb. 2015). DOI: 10.1016/j.carbon.2015.02.045.

[40] C. N. R. Rao and Rahul Sen. “Large aligned-nanotube bundles from ferrocene pyrolysis”. In: *Chem. Commun.* (15 1998), pp. 1525–1526. DOI: 10.1039/A802258E.

[41] Albert Nasibulin et al. “Simple and Rapid Synthesis of α-Fe2O3 Nanowires Under Ambient Conditions”. In: *Nano Research* 2 (May 2010), pp. 373–379. DOI: 10.1007/s12274-009-9036-5.

[42] Néel, M. Louis. “Propriétés magnétiques des ferrites ; ferrimagnétisme et antiferromagnétisme”. In: *Ann. Phys.* 12.3 (1948), ”137–198”. DOI: 10.1051/anphys/194812030137.

[43] C.W. Oatley, W.C. Nixon, and R.F.W. Pease. “Scanning Electron Microscopy”. In: *Advances in Electronics and Electron Physics*. Ed. by L. Marton. Vol. 21. Academic Press, 1966, pp. 181–247. DOI: https://doi.org/10.1016/S0065-2539(08)61010-0.

[44] Özden Özdemir, David J. Dunlop, and Bruce M. Moskowitz. "The effect of oxidation on the Verwey transition in magnetite". In: *Geophysical Research Letters* 20.16 (1993), pp. 1671–1674. DOI: https://doi.org/10.1029/93GL01483. eprint: https://agupubs.onlinelibrary.wiley.com/doi/pdf/10.1029/93GL01483.

[45] P. Paufler. "R. A. Young (ed.). The Rietveld Method. International Union of Crystallography. Oxford University Press 1993. 298 p. Price £ 45.00. ISBN 0–19–855577–6". In: *Crystal Research and Technology* 30.4 (1995), pp. 494–494. DOI: https://doi.org/10.1002/crat.2170300412. eprint: https://onlinelibrary.wiley.com/doi/pdf/10.1002/crat.2170300412.

[46] R Saito, G Dresselhaus, and M S Dresselhaus. *Physical Properties of Carbon Nanotubes*. PUBLISHED BY IMPERIAL COLLEGE PRESS and DISTRIBUTED BY WORLD SCIENTIFIC PUBLISHING CO., 1998. DOI: 10.1142/p080. eprint: https://www.worldscientific.com/doi/pdf/10.1142/p080.

[47] Rahul Sen, A. Govindaraj, and C.N.R. Rao. "Carbon nanotubes by the metallocene route". In: *Chemical Physics Letters* 267.3 (1997), pp. 276–280. ISSN: 0009-2614. DOI: https://doi.org/10.1016/S0009-2614(97)00080-8.

[48] Lyubomir Slavov et al. "Raman spectroscopy investigation of magnetite nanoparticles in ferrofluids". In: *Journal of Magnetism and Magnetic Materials - J MAGN MAGN MATER* 322 (Jan. 2010). DOI: 10.1016/j.jmmm.2010.01.005.

[49] SpaldinNA. *Magnetic Materials : Fundamentals and Applications. 2nd ed.* Cambridge University Press, 2011.

[50] Andreas Thess et al. "Crystalline Ropes of Metallic Carbon Nanotubes". In: *Science (New York, N.Y.)* 273 (Aug. 1996), pp. 483–7. DOI: 10.1126/science.273.5274.483.

[51] Luis Alfonso Torres-Gómez, Guadalupe Barreiro-Rodríguez, and Francisco Méndez-Ruíz. "Vapour pressures and enthalpies of sublimation of ferrocene, cobaltocene and nickelocene". In: *Thermochimica Acta* 124 (1988), pp. 179–183.

[52] Friedrich Walz. "The Verwey transition - a topical review". In: *Journal of Physics: Condensed Matter* 14.12 (Mar. 2002), R285. DOI: 10.1088/0953-8984/14/12/203.

[53] Uhland Weissker et al. "Carbon Nanotubes Filled with Ferromagnetic Materials". In: *Materials* 3.8 (2010), pp. 4387–4427. ISSN: 1996-1944. DOI: 10.3390/ma3084387.

[54] Boris I. Yakobson and Phaedon Avouris. "Mechanical Properties of Carbon Nanotubes". In: *Carbon Nanotubes: Synthesis, Structure, Properties, and Applications*. Berlin, Heidelberg: Springer Berlin Heidelberg, 2001, pp. 287–327. ISBN: 978-3-540-39947-6. DOI: 10.1007/3-540-39947-X_12.

[55] Nan Yan et al. “Fe2O3 Nanoparticles Wrapped in Multi-walled Carbon Nanotubes With Enhanced Lithium Storage Capability”. In: *Scientific reports* 3 (Dec. 2013), p. 3392. DOI: 10.1038/srep03392.

[56] Quan Yang et al. “Electrical Conductivity of Multiwall Carbon Nanotube Bundles Contacting with Metal Electrodes by Nano Manipulators inside SEM”. In: *Nanomaterials* 11.5 (2021). ISSN: 2079-4991. DOI: 10.3390/nano11051290.

[57] Xixian Yang et al. “Enhanced Catalytic Activity of Carbon Nanotubes for the Oxidation of Cyclohexane by Filling with Fe, Ni, and FeNi alloy Nanowires”. In: *Australian Journal of Chemistry* 69 (Jan. 2015). DOI: 10.1071/CH15516.

[58] Lim Siang Ying et al. “Continuous production of carbon nanotubes – A review”. In: *Journal of Industrial and Engineering Chemistry* 17.3 (2011), pp. 367–376. ISSN: 1226-086X. DOI: https://doi.org/10.1016/j.jiec.2011.05.007.

[59] Wang Yun and John Yeow. “A Review of Carbon Nanotubes-Based Gas Sensors”. In: *Journal of Sensors* 2009 (Jan. 2009). DOI: 10.1155/2009/493904.

[60] Irina V. Zaporotskova et al. “Carbon nanotubes: Sensor properties. A review”. In: *Modern Electronic Materials* 2.4 (2016), pp. 95–105. ISSN: 2452-1779. DOI: https://doi.org/10.1016/j.moem.2017.02.002.

[61] Mariusz Zdrojek et al. “Studies of Multiwall Carbon Nanotubes Using Raman Spectroscopy and Atomic Force Microscopy”. In: *Solid State Phenomena* 99 (July 2004), pp. 265–268. DOI: 10.4028/www.scientific.net/SSP.99-100.265.

[62] M Ziese and H J Blythe. “Magnetoresistance of magnetite”. In: *Journal of Physics: Condensed Matter* 12.1 (Jan. 2000), p. 13. DOI: 10.1088/0953-8984/12/1/302.